

Appreciating mergers for understanding the non-linear $M_{\text{bh}}-M_{*,\text{spheroid}}$ and $M_{\text{bh}}-M_{*,\text{galaxy}}$ relations, updated herein, and the implications for the (reduced) role of AGN feedback

Alister W. Graham^{1*}, Nandini Sahu^{1,2}

¹ Centre for Astrophysics and Supercomputing, Swinburne University of Technology, Hawthorn, VIC 3122, Australia

² OzGrav-Swinburne, Centre for Astrophysics and Supercomputing, Swinburne University of Technology, Hawthorn, VIC 3122, Australia

Accepted XXX. Received YYY; in original form ZZZ

ABSTRACT

We present revised (black hole mass)-(spheroid stellar mass) and (black hole mass)-(galaxy stellar mass) scaling relations based on colour-dependent (stellar mass)-to-light ratios. Our 3.6 μm luminosities were obtained from multicomponent decompositions, which accounted for bulges, discs, bars, ansae, rings, nuclear components, etc. The lenticular galaxy bulges (not associated with recent mergers) follow a steep $M_{\text{bh}} \propto M_{*,\text{bulge}}^{1.53 \pm 0.15}$ relation, offset by roughly an order of magnitude in black hole mass from the $M_{\text{bh}} \propto M_{*,\text{ellip}}^{1.64 \pm 0.17}$ relation defined by the elliptical (E) galaxies which, in Darwinian terms, are shown to have evolved by punctuated equilibrium rather than gradualism. We use the spheroid (i.e., bulge and elliptical) size-mass relation to reveal how disc-galaxy mergers explain this offset and the dramatically lower $M_{\text{bh}}/M_{*,\text{sph}}$ ratios in the elliptical galaxies. The deceptive near-linear $M_{\text{bh}}-M_{*,\text{sph}}$ ‘red sequence’, followed by neither the bulge population nor the elliptical galaxies, is shown to be an artefact of sample selection, combining bulges and elliptical galaxies from disparate $M_{\text{bh}}-M_{*,\text{sph}}$ sequences. Moreover, both small bulges with ‘undermassive’ black holes and big lenticular galaxies (including relic ‘red nuggets’) with ‘overmassive’ black holes — relative to the near-linear $M_{\text{bh}}-M_{*,\text{sph}}$ sequence — are no longer viewed as outliers. We confirm a steep $M_{\text{bh}} \propto M_{*,\text{bulge}}^{2.25 \pm 0.39}$ relation for spiral galaxies and discuss numerous implications of this work, including how mergers, rather than (only) feedback from active galactic nuclei, have shaped the high-mass end of the galaxy mass function. We also explain why there may be no useful $M_{\text{bh}}-M_{*,\text{sph}}-R_{\text{e},\text{sph}}$ plane due to $M_{*,\text{sph}}$ scaling nearly linearly with $R_{\text{e},\text{sph}}$.

Key words: galaxies: bulges – galaxies: elliptical and lenticular, cD – galaxies: structure – galaxies: interactions – galaxies: evolution – (galaxies:) quasars: supermassive black holes

1 INTRODUCTION

The linear $M_{\text{bh}}-M_{*,\text{sph}}$ relation (Dressler & Richstone 1988; Dressler 1989), see also Yee (1992), sometimes referred to as the Magorrian relation (Magorrian et al. 1998), has repeatedly been heralded as a critical ingredient to understanding the coevolution of galaxies and their central massive black holes. Black hole feedback is said to regulate the gas and thereby control the star formation (e.g., Silk & Rees 1998; Sijacki et al. 2007; Di Matteo et al. 2008; Schaye et al. 2010; Gaspari et al. 2013, and references therein) and thus establish/explain the $M_{\text{bh}}-M_{*,\text{sph}}$ relation.¹ Despite early evidence for a non-linear $M_{\text{bh}}-M_{*,\text{sph}}$ relation (e.g., Laor 1998, 2001;

Wandel 1999; Salucci et al. 2000), there has been a tendency to cling to the simplicity of the original trend. However, along with increases in sample size and improvements in galaxy decomposition — which have led to both a better understanding of galaxies and a better measurement of their spheroidal component² —, has come an ever-refined insight into the $M_{\text{bh}}-M_{*,\text{sph}}$ diagram through the detection of (galaxy morphology)-dependent substructure and departures from the near-linear relation.

Clues that something was amiss with the notion of a near-linear $M_{\text{bh}}-M_{*,\text{sph}}$ relation were presented in Graham (2012), which reported a steeper near-quadratic relation for spheroids with a Sérsic (1963) light profile³ and a near-linear relation for spheroids with

* E-mail: AGraham@swin.edu.au

¹ Ferrarese & Ford (2005), Longair (2006) and Graham (2016b) review the discovery of black holes and their scaling relations.

² We use the term ‘spheroid’ to denote bulges and (pure) elliptical galaxies.

³ A review of the Sérsic (1963) model can be found in Graham & Driver (2005).

a core-Sérsic light profile⁴ (Graham et al. 2003). This work built on a key tip-off in the final paragraph of Graham (2007)⁵ and was later expressed as a (cool gas)-rich versus (cool gas)-poor galaxy sequence in Graham & Scott (2013) and Scott et al. (2013). Graham & Scott (2015) revealed that the near-quadratic relation also appeared to encompass active galactic nuclei (AGNs) with virial masses⁶ as low as $2 \times 10^5 M_\odot$. With improved data, Savorgnan et al. (2016) found that the distributions in the $M_{\text{bh}}-M_{*,\text{sph}}$ diagram were better described by a ‘blue sequence’ for late-type galaxies (LTGs) — which are all Sérsic galaxies — and a ‘red sequence’ for early-type galaxies (ETGs), which can be Sérsic galaxies or core-Sérsic galaxies. This red versus blue sequence was later emphasised by others, including van den Bosch (2016) and Dullo et al. (2020).

Doubling the sample size of spiral galaxies used by Savorgnan et al. (2016), Davis et al. (2019) could better constrain the $M_{\text{bh}}-M_{*,\text{sph}}$ relation for the LTGs, finding a slope of 2.17 ± 0.32 to $2.44^{+0.35}_{-0.31}$ depending on the regression analysis used. Doubling the sample size of ETGs used by Savorgnan et al. (2016), Sahu et al. (2019a) measured a slope of 1.27 ± 0.07 for the ETGs but crucially explained why this was misleading. Sahu et al. (2019a), and Savorgnan & Graham (2016), knew which ETGs were (pure) elliptical galaxies and which were lenticular or elliptical⁷ galaxies. Separating the ETGs into those with and without discs, Sahu et al. (2019a) revealed that they followed separate $M_{\text{bh}}-M_{*,\text{sph}}$ relations with similar slopes ($\approx 1.9 \pm 0.2$, based on $M_*/L_{3.6} = 0.6$) but offset by an order of magnitude in M_{bh} . Therefore, as Sahu et al. (2019a) explained, published slopes for the near-linear $M_{\text{bh}}-M_{*,\text{sph}}$ relation, i.e., the ‘red-sequence’, are dependent on the sample’s arbitrary number of ETGs with and without discs. See, for example, Graham (2007, with a slope of 0.93 ± 0.10), Kormendy & Ho (2013, with a slope of 1.16 ± 0.08), Saglia et al. (2016, with a slope of 0.846 ± 0.064), and Savorgnan et al. (2016, with a slope of 1.04 ± 0.10). The slope is not a measure of physical importance — as has been thought and reported for over a quarter of a century regarding galaxy/black hole coevolution — but rather a reflection of the sample selection. This revelation has been shown to impact black hole correlations involving not just the spheroid’s stellar mass but also the spheroid’s size (Sahu et al. 2020) and the spheroid’s range of density measures (Sahu et al. 2022a).

This new knowledge is important because it rewrites our understanding of the interplay between spheroids and their central massive black holes. This realisation was refined by performing multicomponent decompositions of the galaxy light, with recourse to kinematic information and accounting for distinct physical entities such as bars, rings, bulges, and discs detected in the images and the Fourier harmonic analysis of the isophotes (Ciambur 2015). Here, with updated data, we offer a likely explanation for the offset between the relations followed by elliptical and elliptical/lenticular galaxies. We also raise some of the ensuing implications. In partic-

ular, we more clearly elucidate the origin and ‘red herring’ nature of the near-linear $M_{\text{bh}}-M_{*,\text{sph}}$ relation in regard to understanding the (limited caretaker) role for AGN feedback in elliptical galaxies.

We previously used a simple conversion of starlight-to-mass in our (galaxy morphology)-dependent scaling diagrams: specifically, $M_*/L_{*,3.6\mu\text{m}} = 0.6$ (Meidt et al. 2014).⁸⁹ Such an approach meshes well with the notion that many compact ‘red nuggets’ at redshifts $z \sim 2.5 \pm 1$ (both massive and not so massive) have become the bulges of some of today’s lenticular and spiral galaxies (Graham et al. 2015; de la Rosa et al. 2016; Graham et al. 2017; Hon et al. 2022a). Such an origin for these bulges would make them old, as Peletier & Balcells (1996) and MacArthur et al. (2009) reported, and therefore require a high mass-to-light ratio. However, not every bulge needs to be old. Here we explore colour-dependent $M_*/L_{\text{obs},3.6}$ ratios for a sample of ~ 100 galaxies pre-observed with the Spitzer Space Telescope and close enough to resolve their bulges ($R_e \gtrsim 2''$). That is, we allow for departures from the assumption that all the bulges have the same $M_*/L \equiv Y_*$ ratio. Here, we use a $B-V$ colour-dependent mass-to-light ratio prescription to derive the stellar masses. Appendix A offers an alternative optical-NIR prescription for the Y_* ratio based on the $V-[3.6]$ colour. It provides an analysis less sensitive to star formation (given that star formation may be more reflective of the disc than the spheroid).

In Section 2, we summarise the salient features of our galaxy sample and describe the prescription for deriving their colour-dependent $M_*/L_{\text{obs},3.6}$ ratios. We have also updated a few black hole masses, some spheroid luminosities, and many galaxy distances, slightly impacting the black hole masses and absolute magnitudes. We provide a data table of final values with sufficient information to trace the origin of the data readily. In Section 3, we present the $M_{\text{bh}}-M_{*,\text{sph}}$ and $M_{\text{bh}}-M_{*,\text{gal}}$ diagrams and relations as a function of galaxy morphology (E, ES/S0, and S).

Section 3.3 presents the size-mass relation for our sample of spheroids and uses this to reveal how dry mergers, and the transition from bulges to E galaxies, naturally produce the offset $M_{\text{bh}}-M_{*,\text{sph}}$ and $M_{\text{bh}}-R_{e,\text{sph}}$ relations for E galaxies relative to the bulges in ES/S0 galaxies and also the offset between ES/S0 and E galaxies in the $M_{\text{bh}}-M_{*,\text{gal}}$ diagram. Section 4.1 explains the apparent over-massive and under-massive black holes (in bulges) relative to the original near-linear relation, with Section 4.1.1 presenting the location of relic ‘red nuggets’ at the top of the bulge sequence. The stripped S0 galaxy M32 — the prototype for the ‘compact elliptical’ galaxy class — is discussed in Section 4.2. Section 4.3 identifies and discusses what may be the primary bivariate black hole relation in the $M_{\text{bh}}-M_{*,\text{sph}}$ diagram. Section 4.4 then discusses the galaxy stellar mass function and the (moot) role of AGN feedback in shaping it instead of potentially just maintaining it. Finally, several other implications are briefly mentioned in Section 4.5.

It is important to note that the authors have been mindful of using the strict interpretation of morphological terms in this paper. An elliptical (E) galaxy has no substantial disc other than perhaps a small nuclear disc, whereas elliptical (ES) and lenticular (S0) galaxies have an intermediate-scale and a large-scale disc, respectively. The expression ‘early-type galaxy’ (ETG) is used to generically refer to the E, ES, and S0 galaxies without a spiral pattern, while

⁴ King & Minkowski (1966) and King & Minkowski (1972) noted that such galaxies have shallow inner light profiles notably flatter than expected from their outer $R^{1/4}$ -like light profile.

⁵ Graham (2012) noted that the final exponent in the second last sentence of the Appendix of Graham (2007) should have read $1/0.5$ rather than 0.5 to give $M_{\text{bh}} \propto L^{1/0.5}$.

⁶ Virial masses were derived using a virial factor $f = 2.8$ (Graham et al. 2011).

⁷ Elliptical galaxy is the name given by Graham et al. (2016b) to the ES galaxy type introduced by Liller (1966). They have intermediate-scale discs which do not dominate the light at large radii, in contrast to the familiar lenticular (S0) galaxies whose large-scale discs do (Graham 2019).

⁸ This was based on a Chabrier (2003) ‘initial mass function’.

⁹ In practice, while $M_*/L_{\text{obs},3.6} = 0.6$ was used for the ETGs (Sahu et al. 2019a), a lower value of $M_*/L_{\text{obs},3.6} = 0.453$ was applied to the LTGs (Davis et al. 2019) because the observed luminosity at $3.6 \mu\text{m}$ includes both starlight and the glow of warm dust. This reduced ratio encapsulated the mean ratio $L_{*,3.6}/L_{\text{obs},3.6} \approx 0.75$ for LTGs (Querejeta et al. 2015).

the expression ‘late-type galaxy’ (LTG) refers to spiral (S) and irregular (Irr) galaxies. This notation is confined to high-surface brightness galaxies that define the galaxy classification grid seen in [Graham \(2019\)](#) and built on the Aitken-Jeans-Lundmark-Hubble galaxy sequence discussed there. The term ‘spheroid’ refers to both an elliptical galaxy and the bulge of a disc galaxy, while the term bulge refers to the bulges of S, ES, and S0 galaxies but not E galaxies. The only (mild) confusion¹⁰ to this nomenclature is that we will sometimes refer to relic ‘red nuggets’ — unevolved spheroidal-shaped galaxies from $z \sim 2.5 \pm 1$ which have not acquired a large-scale disc of stars by today — as belonging to the bulge sequence. Why we do this will become apparent as one reads on.

2 DATA AND ANALYSIS

2.1 The sample

[Davis et al. \(2019\)](#) and [Sahu et al. \(2019a\)](#) provide galaxy decompositions for LTGs and ETGs with directly measured black hole masses obtained from the literature. The galaxy decomposition process involved the extraction of a nested set of one-dimensional profiles, including the surface brightness profile, the ellipticity profile, the position angle profile, and an array of profiles quantifying the amplitude of Fourier Harmonic terms used to describe the isophotal deviations from perfect ellipses ([Ciambur 2015](#)). These one-dimensional profiles enable accurate two-dimensional reconstruction of the galaxy without stochastic irregularities due to, for example, star formation or undigested neighbours. Such irregularities remain in the ‘residual image’, obtained by subtracting the smooth reconstruction from the original image, where they can more readily be studied without the (often overwhelming) glow of the host galaxy (e.g., [Graham et al. 2021](#)). The surface brightness profile of the geometric-mean axis¹¹ is then recreated by optimally fitting a suite of galaxy components. One of the advantages of this approach is that it is not limited to models in which galaxy components may have fixed ellipticity and position angles, as with directly fitting the two-dimensional image. For instance, a single-component triaxial bulge with a radially-varying ellipticity and position angle profile might get broken into two or more components when attempting to model it in two dimensions.

The bulk of the sample was previously imaged with the Spitzer Space Telescope at a wavelength of $3.6 \mu\text{m}$. The galaxies were ‘disassembled’ to reveal their components and better establish the luminosity of their spheroidal component. Their samples were supplemented by using optical and near-IR K_s -band images when the Spitzer data were either unavailable or when better spatial resolution was required to probe the bulge component. To keep things simple, and minimise the introduction of possible biases, here we avoid potential offsets arising from the use of a range of filters and thus adopted stellar mass-to-light ratios. We do this by solely using the galaxy sample whose structural composition was studied at

$3.6 \mu\text{m}$. This sample consists of 73 ETGs¹² plus 31 LTGs¹³, coming from the larger sample of 84 ETGs ([Sahu et al. 2019a](#)) and 43 LTGs ([Davis et al. 2019](#)). The smaller fraction of LTGs with useful Spitzer data is a consequence of the need to resolve the bulge component of the galaxy. As such, more LTGs than ETGs had previously required Hubble Space Telescope (HST) data.

In passing, it is noted that the (peanut shell)-shaped structures associated with buckled bars ([Combes & Sanders 1981](#); [Athanasoulas 2005](#); [Ciambur & Graham 2016](#)) — sometimes referred to as ‘pseudobulges’ — were either modelled as a ‘barlens’ (e.g., [Laurikainen et al. 2011](#); [Sahu et al. 2019a](#), their Figure 3) or effectively folded into the Ferrers bar component during the galaxy decomposition, which can be seen for every galaxy in [Savorgnan & Graham \(2016\)](#), [Davis et al. \(2019\)](#) and [Sahu et al. \(2019a\)](#). As noted above, we revisited the decomposition of seven of these (73+31=) 104 galaxies in [Graham & Sahu \(2022\)](#), and we use the results here.

The distances, shown in Table 1, are regarded as luminosity distances. As such, the small correction for cosmological surface brightness dimming, $2.5\log(1+z)^4$ is (implicitly) applied when we convert the $3.6 \mu\text{m}$ apparent magnitudes, m — given in the above four papers — into absolute magnitudes, \mathcal{M} , using the expression $m - \mathcal{M} = 25 + 5 \log D_L$, where D_L is the luminosity distance in Mpc. No Galactic extinction correction has been applied to the $3.6 \mu\text{m}$ data because any excess emission from dust in the Milky Way glowing at $3.6 \mu\text{m}$ would have effectively been removed during the sky-subtraction procedure (see Section 2.2.1 in [Sahu et al. 2019a](#)). Finally, no K-correction or evolutionary corrections were applied given the small redshifts involved, typically $z \approx 0.01$ – 0.02 .

The spheroid and galaxy absolute magnitudes were expressed in units of solar luminosity using $\mathcal{M}_{\odot,3.6} = 6.02$ (AB mag), equal to 3.26 (Vega mag). These were then converted into stellar masses using the prescription described in the following subsection. These masses appear in Table 1, along with the references to where one can see each galaxy’s decomposition. These references are also the source for the sizes of the spheroids, quantified using the effective half-light radius, $R_{\text{e,sph}}$, measured along the ‘equivalent axis’, R_{eq} (see footnote 11). The masses for the black holes, updated according to the new galaxy distances, are also provided in Table 1. Unless an update is indicated, the nearly 100 references for these black hole masses can be traced through [Sahu et al. \(2020\)](#).

Following the exclusion of mergers by [Kormendy & Ho \(2013\)](#), we exclude from the upcoming Bayesian linear regressions, but not the plots, one LTG plus four ETGs previously identified by others as somewhat unrelaxed mergers (NGC 2960 plus NGC 1194, NGC 1316, NGC 5018 and NGC 5128). We additionally exclude the stripped galaxy NGC 4342 ([Blom et al. 2014](#)) and the dwarf galaxy NGC 404 (Mirach’s Ghost: [Nguyen et al. 2017](#))¹⁴. NGC 404 is the only galaxy in our sample with $M_{\text{bh}} < 10^6 M_{\odot}$, thereby making it vulnerable to potentially biasing the analyses due to the weight it may have in torquing the regression lines.

¹⁰ [Zwicky \(1966\)](#) pointed out that these elliptical-like galaxies are notably more compact than the more commonly known ‘elliptical galaxies’ — many of which turned out to be lenticular galaxies with large-scale discs.

¹¹ The geometric-mean axis, also known as the ‘equivalent axis’ R_{eq} , is given by the geometric-mean of the major (a) and minor (b) axis. These $R_{\text{eq}} = \sqrt{ab}$ radii are equivalent to a circularised version of a galaxy’s quasi-elliptical isophotes.

¹² This sample of 73 ETGs is comprised of 40 from [Savorgnan & Graham \(2016\)](#), of which three (NGC: 821; 1399; and 3377) are remodelled in [Graham & Sahu \(2022\)](#), plus 33 from [Sahu et al. \(2019a\)](#), of which two (NGC 2787 and NGC 5419) are remodelled in [Graham & Sahu \(2022\)](#).

¹³ [Davis et al. \(2019\)](#), their Table 3) contains 28 galaxies with Spitzer data, including NGC 4395 and NGC 6926 which are bulgeless, and including NGC 224 taken from [Savorgnan & Graham \(2016\)](#). Two of these 28 (NGC 1320 and NGC 4699) are remodelled in [Graham & Sahu \(2022\)](#). A further three galaxies (NGC 2273, NGC 4945 and UGC 3789) from [Savorgnan & Graham \(2016\)](#) are included, taking the tally to 31.

¹⁴ NGC 404 lies within seven arcmin of the second magnitude star Mirach.

The ETG with the suspiciously¹⁵ blue colour of ~ 0.6 in Figure 1 is NGC 1275, although we left this galaxy in the sample as its inclusion/exclusion had no appreciable impact. We also included the rather blue LTG NGC 4303 but needed to exclude NGC 5055 due to its uncertain black hole mass (Blais-Ouellette et al. 2004; Smith et al. 2021a) and Circinus, an unrelaxed S galaxy known to be undergoing considerable starbursts in addition to hosting an AGN. The $B - V = 0.174$ (Vega) colour of Circinus is less than 0.5 and well outside of the applicability range of the M/L equations we are about to introduce. The nine galaxies excluded from the linear regression are marked with a dagger symbol (†) in Table 1, which includes all 104 galaxies initially considered here.

2.2 Stellar mass-to-light ratios

As illustrated by, for example, McGaugh & Schombert (2014, their Figure 1), Zhang et al. (2017, their Section 7), and Sahu et al. (2019a, their Figure 4), the colour-dependent mass-to-light ratio prescriptions from different papers do not agree with each other. Even after correcting for the different assumptions in the stellar population models, the equations from different papers do not agree (McGaugh & Schombert 2014, their Figure 6). Schombert et al. (2019, their Figure 10) present half a dozen $(B - V)$ -dependent relations for the mass-to-light ratio. The relation from Into & Portinari (2013) sits in the middle and is therefore adopted here as a middle ground. In the Appendix, we additionally show the result of adopting the latest relation from Schombert et al. (2022).

We have taken the B_T and V_T total galaxy magnitudes from de Vaucouleurs et al. (1991), as listed in the NASA/IPAC Extragalactic Database (NED)¹⁶, and then corrected these for Galactic extinction based on the near-infrared maps of Schlafly & Finkbeiner (2011), again, as provided by NED. These Johnson-Cousins B and V magnitudes are Vega magnitudes and benefit from having been (i) derived from wide field-of-view imaging from which the sky-background was readily available, and (ii) taken in both the Northern and Southern hemisphere, thereby capturing most of our sample. For three ETGs (NGC 6251, NGC 5252, and NGC 7052), and three LTGs (IC 2560, NGC 253, and NGC 2960), either the B - or the V -band magnitude was not available. For these three ETGs we assigned a $B - V$ colour of 0.9, and for these three LTGs we assigned a $B - V$ colour of 0.7. In passing, we recognise that spheroid colours, rather than galaxy colours, would be advantageous. However, this would encompass considerable additional work, requiring multi-component decomposition of two optical bands. Moreover, while both LTGs and ETGs can have colour gradients — i.e., varying colour with radius, which can be due to the bulge-to-disc transition — our sample is dominated by early-type spirals (Sa–Sb) and early-type galaxies (E–S0) for which the bulge and disc colours within individual galaxies may not be too dissimilar (Peletier & Balcells 1996).

The (Galactic extinction)-corrected $B_T - V_T$ galaxy colour, hereafter $B - V$, is shown in Figure 1 and provided in Table 1. It was used to obtain the stellar mass-to-light ratio at $3.6 \mu\text{m}$ as follows. We started with the $(B - V)$ -dependent expression for the K -band M_*/L_K ratio taken from Table 6 of Into & Portinari (2013). It is based on realistic dusty models, designed for “samples that

include a range of morphologies, intrinsic colours and random inclinations”. It is such that

$$\log(M_*/L_K) = 0.866(B - V) - 0.926, \quad (1)$$

which is reportedly based on the Kroupa (1998) ‘initial mass function’ (IMF)¹⁷, and good for $0.5 < B - V < 1.1$. Into & Portinari (2013) report a ± 0.1 dex (25%) uncertainty on these M_*/L_K ratios. As they noted, the combination of dust attenuation (dimming the optical magnitudes) and reddening (of the $B - V$ colour) somewhat cancel to provide M_*/L_K ratios that are consistent with those derived from their simpler (dust free) galaxy model. This partial nulling behaviour was noted by Bell et al. (2003) and can be seen in Driver et al. (2007, their Fig. 13), when assuming the dust models of Popescu et al. (2000).

Here, we convert Eq. 1 into a $3.6 \mu\text{m}$ equation using the following relation taken from the start of Section 5.6 in Schombert et al. (2019, see their Fig. 7):

$$m_K - m_{3.6} = 0.54 - 0.42(B - V).$$

Taking 2.5 times the logarithm of $(M_*/L_K)L_K = (M_*/L_{3.6})L_{3.6}$ and substituting in this $m_K - m_{3.6}$ colour term, one obtains

$$\log(M_*/L_{3.6}) = 1.034(B - V) - 1.142. \quad (2)$$

While the use of individual $m_K - m_{3.6}$ colours rather than the above mean $(B - V)$ -dependent relation might seem preferable, in practice it can become problematic due to the different method used to determine the total K -band and Spitzer magnitudes (e.g., Scott et al. 2013, their Fig. 2).

As noted above, Into & Portinari (2013) initially derived a colour-dependent M_*/L relation for a less complicated galaxy model based on composite stellar populations. This may be more applicable for the ETGs, and is such that $\log(M_*/L_K) = 1.055(B - V) - 1.066$, for $0.2 < B - V < 1.0$. Morphing this in the same manner as done to Equation 1 gives the relation

$$\log(M_*/L_{3.6}) = 1.223(B - V) - 1.282. \quad (3)$$

In the following subsection, we adjust these expressions (equations 2 and 3) to align them with the Kroupa (2002) IMF.

¹⁵ NGC 1275 resides 13 degrees from the Galactic plane and has ~ 0.6 mag of Galactic extinction in the B -band.

¹⁶ <http://nedwww.ipac.caltech.edu>

¹⁷ The IMF is the histogram of stellar birth masses.

Table 1. Black hole, spheroid and galaxy masses, and spheroid sizes

Galaxy (1)	Type (2)	Dist. (Mpc) (3)	kpc'' (4)	$R_{\text{e, sph, equiv}}$ (kpc) (5)	$\log(M_{\text{bh}}/M_{\odot})$ (6)	$B - V$ (7)	$V - [3.6]$ (8)	$\log(M_{*, \text{ sph}}/M_{\odot})$ (9)	$\log(M_{*, \text{ gal}}/M_{\odot})$ (10)	Ref. (11)
Circinus [†]	S	4.21±0.76 (T08)	0.020	0.46	6.25±0.11	0.174	2.41	9.46±0.29	9.97±0.22	DGC19
IC 1459	E	28.1±3.6 (T01')	0.134	7.68	9.38±0.20	0.966	3.84	11.69±0.17	11.69±0.17	SG16
IC 2560	S	32.9±5.0 (NED ⁱ)	0.157	0.62	6.52±0.11	[0.70]	[3.17]	9.66±0.23	10.69±0.18	DGC19
IC 4296*	E	46.9±3.7 (M00')	0.222	9.12	9.10±0.09	0.954	3.36	11.72±0.14	11.74±0.14	SGD19
NGC 0224	S	0.75±0.03 (R12)	0.004	0.69	8.15±0.16	0.865	3.58	10.23±0.15	11.01±0.13	SG16
NGC 0253	S	3.47±0.11 (R11)	0.017	0.47	7.00±0.30	[0.70]	[3.19]	9.76±0.25	10.71±0.13	DGC19
NGC 0404 [†]	ES/SO	3.06±0.37 (K02)	0.015	0.058	5.74±0.1 [4f]	0.889	2.77	8.03±0.50	9.19±0.16	SGD19
NGC 0524	ES/SO	27.7±1.1 (J21)	0.132	1.10	9.00±0.10	0.977	3.13	10.88±0.15	11.38±0.13	SGD19
NGC 0821	E	23.2±1.8 (T01')	0.111	3.45	7.59±0.17	0.893	2.90	10.84±0.15	10.90±0.14	GS22
NGC 1023	ES/SO	11.0±0.8 (T01')	0.053	0.39	7.62±0.05	0.946	3.15	10.33±0.16	10.89±0.14	SG16
NGC 1097	S	24.8±0.6 (R14)	0.119	1.35	8.38±0.04	0.726	3.52	10.84±0.25	11.42±0.13	DGC19
NGC 1194 [†]	ES/SO	54.1±3.8 (NED)	0.256	0.91	7.82±0.04	0.893	3.61	10.78±0.16	11.01±0.14	SGD19
NGC 1275	E	69.0±9.0 (NED ⁱ)	0.324	17.4	8.88±0.21	0.616	4.04	11.56±0.18	11.60±0.17	SGD19
NGC 1300	S	20.7±1.5 (NED)	0.100	0.74	7.86±0.14	0.654	2.86	9.68±0.20	10.55±0.14	DGC19
NGC 1316 [†]	ES/SO	17.8±5.9 (NED ⁱ)	0.086	1.37	8.16±0.29	0.871	3.60	11.05±0.35	11.69±0.31	SG16
NGC 1320	S	36.8±2.6 (NED)	0.175	0.20	6.77±0.22	0.828	3.50	10.13±0.16	10.70±0.14	GS22
NGC 1332	ES/SO	22.0±1.8 (T01')	0.105	1.89	9.15±0.07	0.932	3.41	11.15±0.15	11.17±0.14	SG16
NGC 1374	ES/SO	19.0±1.1 (T01')	0.091	1.07	8.76±0.05	0.908	3.19	10.30±0.16	10.59±0.13	SGD19
NGC 1398	S	24.8±4.5 (T08)	0.119	1.24	8.03±0.11	0.888	3.36	10.76±0.29	11.44±0.20	DGC19
NGC 1399	E	19.2±1.4 (T01')	0.092	5.71	8.67±0.06	0.949	3.74	11.46±0.16	11.46±0.16	GS22
NGC 1407	E	27.8±3.3 (T01')	0.133	6.29	9.65±0.08	0.969	3.31	11.60±0.17	11.66±0.16	SGD19
NGC 1600	E	71.7±2.7 (J21)	0.336	16.7	10.25±0.04	0.972	3.56	12.06±0.13	12.06±0.13	SGD19
NGC 2273	S	30.3±4.0 (NED ⁱ)	0.145	0.28	6.95±0.06	0.828	3.41	10.35±0.22	10.83±0.17	SG16
NGC 2549	ES/SO	12.2±1.6 (T01')	0.059	0.18	7.15±0.60	0.913	3.19	9.67±0.19	10.21±0.17	SG16
NGC 2778	ES/SO	22.1±3.1 (T01')	0.106	0.23	7.18±0.35	0.911	3.06	9.49±0.23	10.15±0.17	SG16
NGC 2787	ES/SO	7.2±1.2 (T01')	0.035	0.14	7.59±0.09	0.942	3.34	9.37±0.24	10.10±0.19	GS22
NGC 2960 [†]	S	73.0±5.1 (NED)	0.342	0.75	7.07±0.05	[0.70]	[3.34]	10.44±0.16	10.86±0.14	DGC19
NGC 2974	S	21.5±2.5 (T08)	0.103	0.67	8.23±0.07	0.952	3.45	10.48±0.22	10.98±0.16	DGC19
NGC 3031	S	3.48±0.13 (K12)	0.017	0.73	7.83±0.09	0.879	3.21	10.34±0.25	10.83±0.13	DGC19
NGC 3079	S	16.5±2.9 (T08)	0.079	0.34	6.38±0.12	0.670	4.03	9.88±0.29	10.64±0.20	DGC19
NGC 3091	E	58.6±10.9 (T07)	0.276	14.1	9.62±0.08	0.962	3.74	11.86±0.20	11.86±0.20	SG16
NGC 3115	ES/SO	9.3±0.4 (T01')	0.045	1.55	8.94±0.25	0.929	3.30	10.87±0.14	10.95±0.13	SG16
NGC 3227	S	25.7±3.2 (K15)	0.123	1.03	7.97±0.14	0.800	3.19	10.31±0.22	11.07±0.16	DGC19
NGC 3245	ES/SO	20.1±1.9 (T01')	0.097	0.23	8.30±0.12	0.888	3.06	10.12±0.17	10.70±0.15	SG16
NGC 3368	S	10.8±1.5 (NED ⁱ)	0.052	0.25	6.89±0.11	0.838	3.33	9.95±0.17	10.83±0.17	DGC19
NGC 3377	E	10.8±0.4 (T01')	0.052	2.30	7.89±0.03	0.830	3.29	10.30±0.14	10.36±0.13	GS22
NGC 3379	E	10.9±1.6 (K15)	0.053	2.70	8.62±0.13	0.938	3.44	10.97±0.20	10.97±0.20	SG16
NGC 3384	ES/SO	11.2±0.7 (T01')	0.054	0.30	7.23±0.05	0.907	3.33	10.14±0.16	10.67±0.14	SG16
NGC 3414	E	24.3±3.7 (T01')	0.117	2.98	8.38±0.09	0.948	3.39	10.95±0.19	10.98±0.18	SG16
NGC 3489	ES/SO	11.6±0.8 (T01')	0.056	0.095	6.76±0.07	0.816	2.98	9.53±0.20	10.30±0.14	SG16
NGC 3585	E	19.3±1.6 (T01')	0.093	8.03	8.49±0.13	0.914	3.84	11.38±0.15	11.39±0.14	SG16
NGC 3607	E	25.0±3.2 (K15)	0.120	7.86	8.16±0.18	0.911	3.54	11.43±0.17	11.46±0.17	SG16
NGC 3608	E	22.1±1.4 (T01')	0.106	4.60	8.30±0.17	0.922	3.45	10.98±0.14	10.98±0.14	SG16
NGC 3627	S	10.4±1.8 (K15)	0.050	0.20	6.94±0.09	0.701	3.24	9.72±0.21	10.76±0.20	DGC19
NGC 3665	ES/SO	34.7±2.4 (T07)	0.166	2.12	8.76±0.10	0.933	3.54	11.14±0.16	11.39±0.14	SGD19
NGC 3842	E	87.5±4.1 (J21)	0.407	30.0	9.94±0.13	0.941	3.84	11.91±0.14	11.93±0.13	SG16
NGC 3923	E	22.1±2.9 (T01')	0.106	8.35	9.47±0.13	0.929	3.74	11.55±0.17	11.55±0.17	SGD19
NGC 3998	ES/SO	13.6±1.2 (T01')	0.065	0.31	8.33±0.43[4a]	0.936	3.47	10.12±0.26	10.61±0.15	SG16
NGC 4026	ES/SO	13.2±1.7 (T01')	0.063	0.15	8.26±0.12	0.901	3.27	10.19±0.22	10.44±0.17	SGD19
NGC 4151	S	19.0±2.5 (H14)	0.094	0.56	7.69±0.37	0.706	3.44	10.28±0.22	10.62±0.17	DGC19
NGC 4258	S	7.6±0.17 (H13)	0.037	0.98	7.60±0.01	0.676	3.37	10.02±0.19	10.70±0.13	DGC19
NGC 4261	E	30.4±2.7 (T01')	0.145	6.86	9.20±0.09[4b]	0.975	3.69	11.52±0.16	11.54±0.15	SG16
NGC 4291	E	25.2±3.7 (T01')	0.121	1.86	8.51±0.37	0.927	3.38	10.80±0.18	10.80±0.18	SG16
NGC 4303	S	19.3±0.6 (R14)	0.093	0.20	6.78±0.17	0.510	2.90	9.60±0.25	10.66±0.13	DGC19
NGC 4339	ES/SO	15.8±1.3 (T01')	0.076	0.49	7.62±0.33	0.887	2.96	9.73±0.21	10.22±0.14	SGD19
NGC 4342 [†]	ES/SO	22.8±0.8 (B09')	0.110	0.52	8.65±0.18	0.932	3.52	10.04±0.15	10.36±0.15	SGD19
NGC 4350	ES/SO	17.0±0.5 (B15)	0.082	1.59	8.87±0.41	0.926	3.43	10.39±0.25	10.66±0.13	SGD19
NGC 4371	ES/SO	16.4±3.4 (T07)	0.079	0.70	6.84±0.12	0.948	3.34	9.99±0.30	10.70±0.22	SGD19
NGC 4374	E	17.7±0.9 (T01')	0.085	11.0	8.95±0.05	0.944	3.75	11.61±0.15	11.61±0.15	SG16
NGC 4388	S	18.0±3.6 (S14)	0.087	1.24	6.90±0.10	0.711	3.34	10.07±0.30	10.45±0.21	DGC19
NGC 4395	S	4.56±0.17 (S18)	0.022	...	5.62±0.17	0.445	2.96	...	9.15±0.13	DGC19
NGC 4429	ES/SO	16.6±0.8 (C08)	0.080	0.90	8.18±0.08	0.950	3.40	10.60±0.20	11.04±0.13	SGD19

Table 1. Continued

Galaxy (1)	Type (2)	Dist. (Mpc) (3)	kpc'' (4)	$R_{\text{e, sph, equiv}}$ (kpc) (5)	$\log(M_{\text{bh}}/M_{\odot})$ (6)	$B - V$ (7)	$V - [3.6]$ (8)	$\log(M_{*, \text{ sph}}/M_{\odot})$ (9)	$\log(M_{*, \text{ gal}}/M_{\odot})$ (10)	Ref. (11)
NGC 4434	ES/S0	22.3±0.7 (B09')	0.107	0.57	7.85±0.17	0.861	3.07	9.95±0.20	10.22±0.13	SGD19
NGC 4459	ES/S0	15.5±1.6 (T01')	0.075	0.98	7.82±0.10	0.910	3.28	10.56±0.21	10.77±0.15	SG16
NGC 4472	E	15.7±0.7 (T01')	0.075	10.2	9.36±0.04	0.940	3.72	11.75±0.13	11.75±0.13	SG16
NGC 4473	E	15.1±0.9 (T01')	0.073	2.69	8.07±0.36	0.935	3.30	10.75±0.13	10.83±0.13	SG16
NGC 4486	E	16.8±0.8 (EHT)	0.081	7.06	9.81±0.06[4c]	0.940	3.60	11.67±0.15	11.67±0.15	SG16
NGC 4501	S	17.0±0.5 (B15)	0.082	1.67	7.31±0.08	0.696	3.53	10.46±0.25	11.02±0.13	DGC19
NGC 4526	ES/S0	16.3±1.5 (T01')	0.078	1.16	8.65±0.04	0.940	3.38	10.79±0.26	11.13±0.15	SGD19
NGC 4552	E	14.8±1.0 (T01')	0.071	5.08	8.67±0.05	0.944	3.44	11.01±0.16	11.07±0.16	SGD19
NGC 4564	ES/S0	14.4±1.1 (T01')	0.069	0.41	7.77±0.06	0.901	3.20	10.08±0.16	10.35±0.14	SG16
NGC 4578	ES/S0	16.2±0.5 (B09')	0.078	0.49	7.28±0.35	0.842	3.25	9.79±0.15	10.24±0.13	SGD19
NGC 4594	S	9.55±0.44 (Mc16)	0.046	1.90	8.81±0.03	0.935	3.11	11.04±0.25	11.26±0.13	DGC19
NGC 4596	ES/S0	17.0±0.5 (B15)	0.082	0.74	7.90±0.20	0.921	3.37	10.28±0.20	10.86±0.13	SG16
NGC 4621	E	17.6±1.6 (T01')	0.084	7.64	8.59±0.06	0.912	3.56	11.24±0.16	11.28±0.15	SG16
NGC 4649	E	16.2±1.1 (T01')	0.078	6.29	9.66±0.10	0.946	3.58	11.56±0.14	11.56±0.14	SGD19
NGC 4697	E	11.3±0.7 (T01')	0.054	12.2	8.26±0.04	0.884	3.81	11.07±0.15	11.12±0.14	SG16
NGC 4699	S	20.4±3.8 (K13)	0.098	0.23	8.27±0.09	0.860	3.24	10.30±0.25	11.27±0.20	GS22
NGC 4736	S	5.0±0.4 (T01')	0.024	0.23	6.83±0.11	0.735	3.48	10.03±0.21	10.51±0.14	DGC19
NGC 4742	ES/S0	14.9±1.1 (T01')	0.072	0.25	7.13±0.18	0.774	2.91	9.78±0.16	10.07±0.14	SGD19
NGC 4762	ES/S0	17.0±0.5 (B15)	0.082	0.18	7.24±0.14	0.841	3.35	9.74±0.15	10.83±0.13	SGD19
NGC 4826	S	7.2±0.7 (T01')	0.035	0.42	6.18±0.12	0.803	3.31	9.88±0.21	10.74±0.15	DGC19
NGC 4889	E	96.3±6.7 (NED)	0.446	27.1	10.3±0.44	1.031	3.93	12.26±0.14	12.26±0.14	SG16
NGC 4945	S	3.56±0.20 (Mo16)	0.017	0.16	6.13±0.30	[0.70]	[3.09]	9.29±0.20	10.42±0.13	SG16
NGC 5018 [†]	ES/S0	38.4±2.7 (NED)	0.183	1.13	8.00±0.08	0.836	3.10	10.93±0.16	11.31±0.14	SGD19
NGC 5055 [†]	S	8.87±0.39 (M17)	0.043	1.87	8.94±0.10	0.704	3.41	10.49±0.25	10.81±0.13	DGC19
NGC 5077	E	39.8±7.4 (T07)	0.189	4.35	8.85±0.23	0.987	3.60	11.41±0.20	11.41±0.20	SG16
NGC 5128 [†]	ES/S0	3.76±0.05 (K07)	0.018	1.09	7.65±0.12	0.899	3.60	10.71±0.25	11.14±0.12	SG16
NGC 5252	ES/S0	104.0±7.3 (NED)	0.480	0.71	9.03±0.40	[0.90]	[3.42]	10.97±0.27	11.50±0.15	SGD19
NGC 5419	E	57.0±4.0 (NED)	0.269	10.8	9.87±0.14	0.986	3.42	11.87±0.16	11.87±0.14	GS22
NGC 5576	E	24.5±1.6 (T01')	0.118	5.82	8.19±0.10	0.863	3.35	10.90±0.16	10.90±0.16	SG16
NGC 5813	ES/S0	31.0±2.6 (T01')	0.148	2.10	8.83±0.06	0.940	3.17	10.96±0.16	11.34±0.14	SGD19
NGC 5845	ES/S0	25.0±2.4 (T01')	0.120	0.63	8.41±0.22	0.972	3.38	10.26±0.21	10.46±0.15	SGD19
NGC 5846	E	24.0±2.2 (T01')	0.115	9.59	9.04±0.06	0.961	3.79	11.55±0.15	11.55±0.15	SG16
NGC 6251	E	104.6±7.3 (NED)	0.483	14.5	8.77±0.16	[0.90]	[3.62]	11.87±0.15	11.87±0.15	SG16
NGC 6861	ES/S0	27.0±4.0 (T01')	0.129	2.60	9.30±0.08	0.962	3.61	11.07±0.19	11.15±0.18	SGD19
NGC 6926	S	85.6±6.0 (NED)	0.399	...	7.68±0.50 [4d]	0.586	3.02	...	11.13±0.14	DGC19
NGC 7052	E	61.9±2.6 (J21)	0.291	5.83	9.35±0.05[4e]	[0.90]	[3.53]	11.46±0.13	11.46±0.13	SGD19
NGC 7332	ES/S0	22.2±2.0 (T01')	0.106	0.26	7.06±0.20	0.877	3.40	10.17±0.17	10.79±0.15	SGD19
NGC 7457	ES/S0	12.7±1.2 (T01')	0.061	0.40	6.96±0.30	0.843	3.07	9.34±0.17	10.12±0.15	SGD19
NGC 7582	S	22.2±4.0 (N11)	0.106	0.48	7.72±0.12	0.737	3.60	10.28±0.29	10.90±0.20	DGC19
NGC 7619	E	46.6±1.7 (J21)	0.221	12.8	9.36±0.09	0.968	3.69	11.69±0.14	11.71±0.13	SG16
NGC 7768	E	108.2±7.6 (NED)	0.499	21.0	9.09±0.15	0.906	3.83	11.90±0.16	11.90±0.16	SG16
UGC 3789	S	50.7±5.2 (R13)	0.240	0.58	7.07±0.05	[0.70]	[3.27]	10.11±0.26	10.68±0.15	SG16

Column 1: Galaxy name ([†] Excluded from the Bayesian linear regression. * IC 4296 = Abell 3565-BCG). Column 2: Broad galaxy type from [Sahu et al. \(2020, their Table A1\)](#). Column 3: Adopted 'luminosity distance' in Mpc: T01' = [Tonry et al. \(2001\)](#) with a 0.083 mag reduction to their distance moduli (see Section 2.2.1); T08 = [Tully et al. \(2008, 2009\)](#); Y12 = [Yamauchi et al. \(2012\)](#); M00' = [Mei et al. \(2000\)](#) with a 0.083 mag reduction to their distance moduli; R12 = [Riess et al. \(2012\)](#); R11 = [Radburn-Smith et al. \(2011\)](#); K02 = [Karachentsev et al. \(2002\)](#); R14 = [Rodríguez et al. \(2014\)](#); R13 = [Reid et al. \(2013\)](#); NED[†] = median redshift-independent distance from NED (and the standard deviation associated with the *mean* redshift-independent distance); NED = (Virgo + GA + Shapley)-corrected Hubble flow distance based on $H_0 = 73 \text{ km s}^{-1} \text{ Mpc}^{-1}$; T07 = [Theureau et al. \(2007\)](#) mean value via NED; K12 = [Kudritzki et al. \(2012\)](#); K15 = [Karachentsev et al. \(2015\)](#); H14 = [Hönl et al. \(2014\)](#); H13 = [Humphreys et al. \(2013\)](#); B09' = [Blakeslee et al. \(2009\)](#) with a 0.023 mag reduction to their distance moduli (see Section 2.2.1), and using the distance for NGC 4365 in the case of NGC 4342 ([Blom et al. \(2014\)](#)); S14 = [Sorce et al. \(2014\)](#); S18 = [Sabbi et al. \(2018\)](#); C08 = [Cortés et al. \(2008\)](#); EHT = [Event Horizon Telescope Collaboration et al. \(2019a\)](#); Mc16 = [McQuinn et al. \(2016\)](#); Mo16 = [Monachesi et al. \(2016\)](#); B15 = [Boselli et al. \(2015\)](#); K13 = [Karachentsev & Nasonova \(2013\)](#); J21 = [Jensen et al. \(2021\)](#); M17 = [McQuinn et al. \(2017\)](#); K07 = [Karachentsev et al. \(2007\)](#); N11 = [Nasonova et al. \(2011\)](#). Column 4: Scale size conversion based on the 'angular-size distance' (not shown) and using $H_0 = 73 \text{ km s}^{-1} \text{ Mpc}^{-1}$, $\Omega_m = 0.3$ and $\Omega_\Lambda = 0.7$. Column 5: Effective half-light radius of the spheroid, derived from the geometric-mean axis, equivalent to a circularised version of the quasi-elliptical isophotes. Column 6: Black hole masses from the compilation in [Sahu et al. \(2020\)](#), and the reference-chain therein, after adjusting to the distances in Column 3. Exceptions are: 4a = [Devereux \(2018\)](#); 4b = [Boizelle et al. \(2021\)](#); 4c = [Event Horizon Telescope Collaboration et al. \(2019b\)](#); 4d = [Zhao et al. \(2018, upper limit\)](#); 4e = [Smith et al. \(2021b\)](#); and 4f = [Davis et al. \(2020\)](#). Columns 7 and 8: (Galactic extinction)-corrected $B - V$ and $V - [3.6]$ colours, obtained from NED. The former are used in Equation 4 and the latter in the Appendix equation A2, to derive the $3.6 \mu\text{m}$ stellar mass-to-light ratios for calculating the stellar masses. Values in [brackets] are assumed rather than measured. Column 9: Spheroid stellar mass based on the Spitzer apparent magnitude reported by either: SG16 ([Savorgnan et al. \(2016\)](#)); DGC19 ([Davis et al. \(2019\)](#)); SGD19 ([Sahu et al. \(2019b\)](#)); or GS22 ([Graham & Sahu \(2022\)](#)). The revised distances, colour-dependent M_*/L ratios, and updated magnitudes for seven systems presented in GS22, results in the updates, shown here, for the stellar masses reported in [Sahu et al. \(2020\)](#). Column 10: Updated galaxy stellar mass. Column 11: Reference displaying the multicomponent decomposition used to obtain both the spheroid magnitude and size, and the galaxy magnitude.

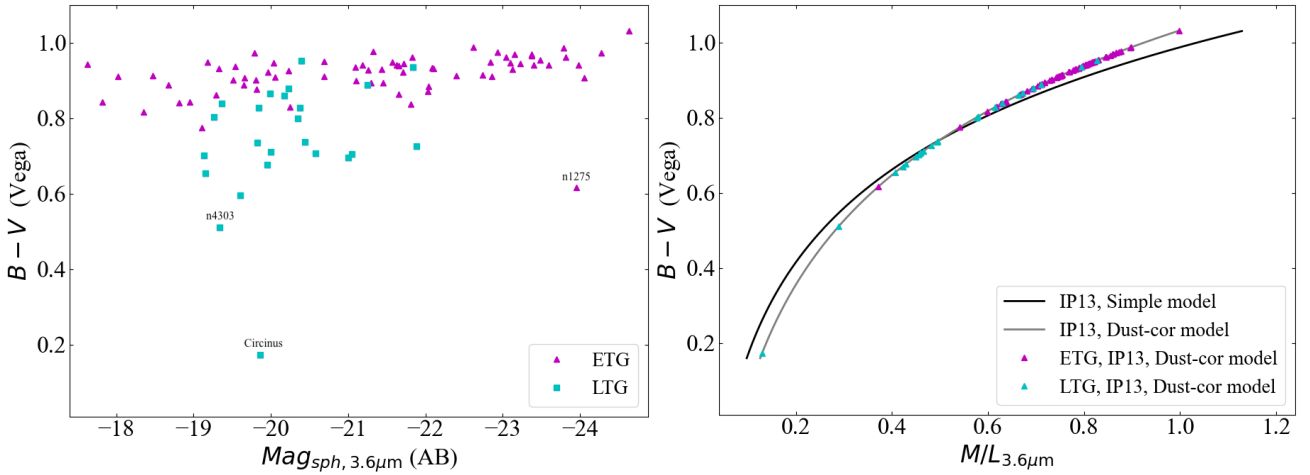


Figure 1. Left-hand panel: (Galactic extinction)-corrected $B - V$ galaxy colour (Vega mag) versus the $3.6 \mu\text{m}$ absolute magnitude $M_{3.6}$ (AB mag) of the spheroid. Both NGC 1275 and Circinus are close to the Galactic plane. Right-hand panel: The thick curve (with the triangles) shows the same $B - V$ colour versus the logarithm of the stellar mass-to-light ratio at $3.6 \mu\text{m}$ obtained from Equation 4, adapted from the dusty galaxy model of [Into & Portinari \(2013, their Table 6\)](#). For reference, we also show with a thin curve their simple galaxy model (their Table 3, our Equation 5). Both models have been converted here to a [Kroupa \(2002\)](#) IMF, see Section 2.2.1 for details. (Circinus falls below the blue-end cut-off of $B - V = 0.5$ for the applicable range of these mass-to-light ratio equations.)

2.2.1 Consideration of the IMF

The stellar mass-to-light ratios from the above, and all, stellar population models are dependent upon the assumed IMF (see [Kroupa et al. 2013](#)). To convert from the [Kroupa \(1998\)](#) IMF¹⁸ (spanning $0.1\text{--}100 M_{\odot}$) — which was used by [Into & Portinari \(2013\)](#) and is inherent in the previous equations — to an alternative IMF, the logarithm of the M_*/L ratio needs to be adjusted by a (near) constant factor (e.g., [Madau & Dickinson 2014](#)). This is shown by [Flynn et al. \(2006, their Figure 12\)](#), where it can be seen that switching to the Salpeter IMF (spanning $0.1\text{--}100 M_{\odot}$)¹⁹ requires adding 0.225 dex to the above equations. Conversion to other assumed IMFs can be done following the offsets provided by, for example, [Bell et al. \(2003, their p.306\)](#) or [Bernardi et al. \(2010, their Table 2\)](#). In this paper, we adopt the [Kroupa \(2002\)](#) IMF, detailed further in [Kroupa et al. \(2013\)](#), and have therefore added 0.225 dex and subtracted 0.30 dex from Eq. 2 to give

$$\log(M_*/L_{3.6}) = 1.034(B - V) - 1.067. \quad (4)$$

Following [Into & Portinari \(2013\)](#), we assign a 25 percent uncertainty to these $M_*/L_{3.6}$ ratios.

In the same way, Equation 3 becomes

$$\log(M_*/L_{3.6}) = 1.223(B - V) - 1.207. \quad (5)$$

We have included this additional relation (Equation 5), shown in the right-hand panel of Figure 1, simply to demonstrate that it yields similar $M_*/L_{3.6} \equiv Y_{*,3.6}$ ratios to those from Equation 4.

We proceed using Equation 4 to derive the spheroid and galaxy stellar masses for all. In Table 1, we list the spheroid and galaxy stellar-masses, and the black hole masses taken from the compilation in [Sahu et al. \(2020\)](#), unless indicated otherwise. The luminosity distances are also tabulated here. Distances from [Tonry et al.](#)

(2001) have been reduced by ~ 4 percent due to a 0.083 mag reduction in their distance moduli. This arose from a 0.06 mag reduction after a recalibration by ([Blakeslee et al. 2002, their Section 4.6](#))²⁰ plus a 0.023 mag reduction due to a reduced distance modulus for the Large Magellanic Cloud ([Pietrzyński et al. 2019](#)) involved in the initial calibration. The black hole masses depend linearly on the angular distance to the host galaxies, and these masses have been updated here to reflect this.

Following [Sahu et al. \(2019a, their Eq. 9\)](#), the quoted uncertainties on the stellar masses include three uncertainties added in quadrature. These relate to the distance (see Table 1), the M_*/L ratio (a 25 percent uncertainty is suggested by [Into & Portinari \(2013\)](#)), and the apparent magnitude. Here, we use a 0.15 mag uncertainty for the galaxy magnitude, and thus also for the spheroidal component of pure elliptical galaxies. This primarily captures uncertainty in the extrapolation of the light profile to large radii ([Graham & Driver 2005, their Figure 1](#)) and this value also falls in the middle of the -0.11 to $+0.18$ range reported by [Savorgnan & Graham \(2016, their Section 4.2.4\)](#). For those galaxies with two or more components, we assign uncertainties reflecting the complexity of the decomposition and thus the accuracy of the spheroid magnitude. These uncertainties were at elevated levels in [Savorgnan & Graham \(2016\)](#) and, in turn, [Sahu et al. \(2019a\)](#) because they were based on the published range of spheroid magnitudes from decompositions that, in retrospect, were clearly in error due to, for example, missed discs or bars. Having narrowed in on a better suite of components for each galaxy, the typical uncertainty on the spheroid magnitude is reduced. We adopt the following grading schema for the uncertainties on the magnitudes: Grade 0 (0.15 mag: single-component galaxy); Grade 1 (0.2 mag: ES galaxies and those with only minor inner components); Grade 1.5 (0.25 mag: typically a clean bulge+disc fit, or if several arcseconds of inner data were excluded, or if intracluster light (ICL) is present); Grade 2 (0.40 mag: usually a bar+bulge+disc fit); Grade 3 (0.55 mag: typically many

¹⁸ The concluding section in [Kroupa \(1998\)](#) notes an IMF slope $\alpha_1 = 1.3$, and $\alpha_2 = 2.2$ from their previous sections, along with $\alpha_3 = 2.7$ for representing the IMF of the Galactic field.

¹⁹ The mass limits within which the IMF used by [Into & Portinari \(2013\)](#) was integrated are stated in [Portinari et al. \(2004\)](#).

²⁰ We opt not to use the attempted refinement offered by Equation A1 and Figure 7 in [Blakeslee et al. \(2010\)](#).

components present). The forthcoming regressions were, however, tested and found to be stable (at the 1σ level) to a broad range of uncertainties.

In Appendix A, we repeat the forthcoming analysis of Section 3 using an alternative optical-infrared colour-dependent prescription for the mass-to-light ratio, taken from Schombert et al. (2022). This additional analysis supports one of our primary conclusions: that violent, disc-destroying, mergers of (red) bulge+disc galaxies (e.g., Naab et al. 2006) produce an offset population of elliptical galaxies in the $M_{\text{bh}}-M_{*,\text{sph}}$ diagram. Neither the initial (bulge) nor the secondary (elliptical galaxy) relations have a near-linear slope in this diagram.

3 RESULTS

3.1 The $M_{\text{bh}}-M_{*,\text{spheroid}}$ and $M_{\text{bh}}-M_{*,\text{galaxy}}$ diagrams

In Figure 2, we show the $M_{\text{bh}}-M_{*,\text{sph}}$ diagram, using Equation 4, for the three morphological types: E, ES/S0 and S. In the upper panel we combine the E, ES and S0 galaxies, which represent the ETGs. In the middle panel, there is no grouping of the different galaxy types, while in the lower panel, we combine the ES, S0 and S galaxies, representing the disc galaxies. The first point we make is that the slope of the $M_{\text{bh}}-M_{*,\text{sph}}$ relation for bulges in either S galaxies or ES/S0 galaxies, and the slope of the $M_{\text{bh}}-M_{*,\text{sph}}$ relation for elliptical galaxies, is neither equal to 1 nor close to it. This is quantified in Table 2 and described further in Section 3.2.

The different relations for the bulges and elliptical galaxies can also be seen in the $(M_{\text{bh}}/M_{*,\text{sph}})-M_{*,\text{sph}}$ diagram (Figure 3). For a given spheroid stellar-mass, Figure 3 reveals different $(M_{\text{bh}}/M_{*,\text{sph}})$ ratios for elliptical galaxies and the bulges of disc galaxies. This different ratio has received little attention in the literature and has never been explained. The arrows in this diagram trace the expected movement due to simple, equal-mass, dry mergers of galaxies with some illustrative bulge-to-total stellar mass ratios, B/T . The merger of two E galaxies produces a shift to the right, while a merger of two identical S0 galaxies with a typical $B/T = 0.25$ (e.g., Laurikainen et al. 2005) produces a considerable shift to the lower right. Considering the mean regression lines, the elliptical galaxies appear to be built, on average, by just one major merger. One can also appreciate how brightest cluster galaxies (BCGs), which are typically E galaxies, occupy the right-hand side of the distribution in this diagram.

Figure 4 shows, for different morphological types, the trend between black hole mass and B/T , or more precisely, the spheroid-to-total stellar mass ratio. B/T is not some near-constant value for all S0 galaxies; a range of ratios is known (e.g., Graham & Worley 2008). Aside from the exclusions mentioned in Section 2.1, here we exclude the ES/S0 galaxy NGC 4762 given the excessive weight its small B/T ratio has on our sample's regression.²¹ Figure 4 reveals that the S0 galaxies with the lower B/T ratios have smaller black hole masses, as is observed among the S galaxies. These trends aid our understanding of the transition from the $M_{\text{bh}}-M_{*,\text{sph}}$ diagram (Figure 2) to the $M_{\text{bh}}-M_{*,\text{gal}}$ diagram (Figure 5). For a given black hole mass, the smaller B/T ratios in the LTGs imply that there will be a steeper $M_{\text{bh}}-M_{*,\text{gal}}$ relation for LTGs than for ES/S0 galaxies. That is, given the greater disc-to-bulge flux ratios and smaller

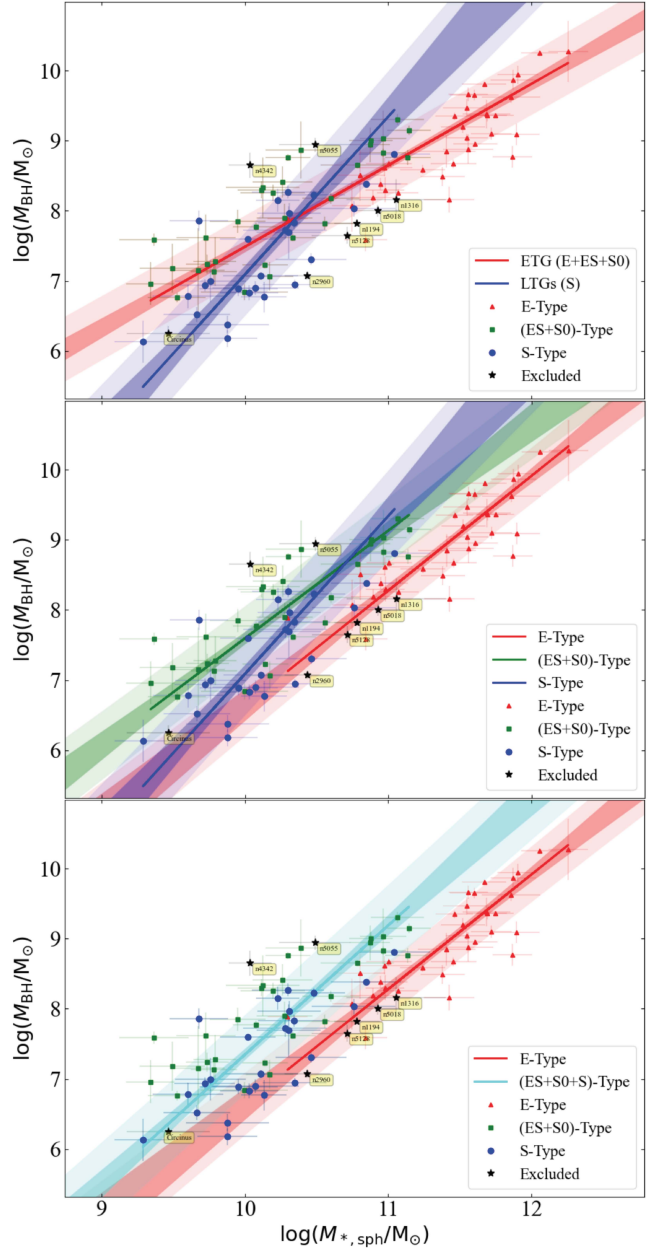


Figure 2. Black hole mass versus spheroid stellar mass (obtained via Equation 4) for different galaxy morphologies (E, ES/S0 and S). As noted in the inset legends, each panel sampled the galaxies differently. The darker shading reveals the 1σ uncertainty on each relations' slope and intercept — as determined by ‘confband.py’ from SciPy (Virtanen et al. 2020) —, while the lighter shading shows the root mean square (rms) scatter. All quantities are shown in Table 2. The middle panel reveals that the single relation for ETGs, shown in the upper panel, overlooks a key division between ETGs with and without discs. Similarly, the single relation for disc galaxies, shown in the lower panel, overlooks the division between disc galaxies with and without a spiral pattern and thus the varying abundance of cold gas and star formation. While one may use Table 1 to identify every galaxy shown here, for some galaxies mentioned in the text, we have added small labels which can be seen by zooming in. These are small to avoid overly detracting from the underlying patterns.

²¹ We do not wish to imply that S0 galaxies with low B/T ratios are in error, only that this B/T data point for NGC 4762 interferes with the current mapping between Figures 2 and 5.

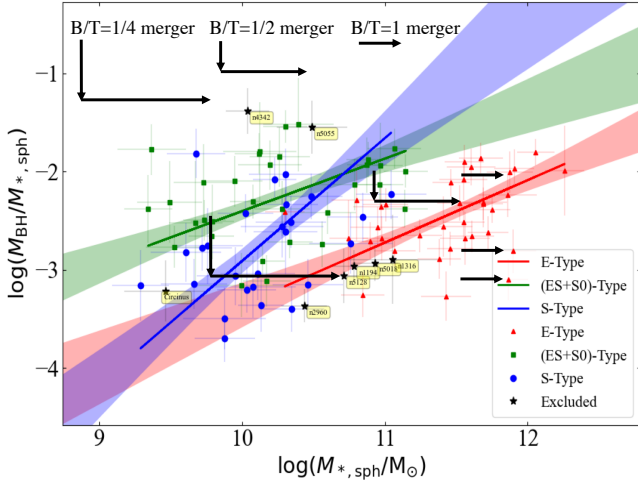


Figure 3. $M_{\text{bh}}/M_{*,\text{sph}}$ mass ratio versus $M_{*,\text{sph}}$. We have mapped the lines, and their 1σ uncertainty, from the middle panel of Figure 2. For a given spheroid mass, the mean $M_{\text{bh}}/M_{*,\text{sph}}$ ratio is different by roughly an order of magnitude for ETGs with and without discs. As shown by the arrows, equal-mass mergers of S0 galaxies (illustrated here with two different bulge-to-total stellar mass ratios, $B/T = 1/4$ and $1/2$) can shift systems towards the lower right. For example, an E galaxy built from an equal-mass merger of two S0 galaxies with $B/T = 1/2$ will enact both a downward shift of ~ 0.3 dex ($= \log 2$) and a rightward shift of ~ 0.6 dex ($= \log 4$). Given the slope of 0.53 ± 0.15 for the distribution of ES/S0 galaxies in this diagram, equal-mass mergers between S0 galaxies with $B/T = 1/2$ (or $= 1/4$) will create a new relation with a vertical offset of ~ 0.6 (or ~ 0.8) dex. On the other hand, equal-mass mergers of E galaxies with $B/T = 1$ will create a remnant shifted to the right by only ~ 0.3 dex, as shown by the three example arrows.

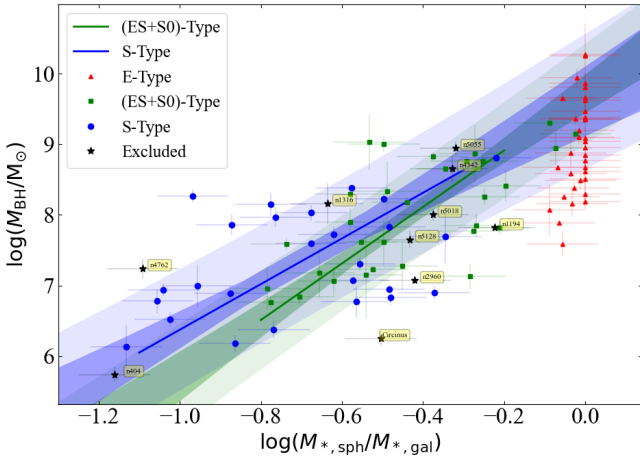


Figure 4. Black hole mass versus the logarithm of the spheroid-to-total stellar mass ratio for S, ES/S0 and E galaxies (for which the ratio tends to 1). The symbols and shading have the same meaning as in Figure 2. To help understand the transition from the $M_{\text{bh}}-M_{*,\text{sph}}$ diagram (Figure 2) to the $M_{\text{bh}}-M_{*,\text{gal}}$ diagram (Figure 5), we have shown how the ‘spheroid-to-total’ ratio relates to the black hole mass. A linear regression of $M_{*,\text{sph}}/M_{*,\text{gal}}$ and M_{bh} has been performed here (see Table 2). Note: Some E galaxies have B/T ratios smaller than some ES galaxies due to additional undigested components and/or nuclear discs.

spheroid masses when moving from Sa to Sc galaxies, the spiral galaxies transition to a steeper $M_{\text{bh}}-M_{*,\text{gal}}$ relation than the early-type disc galaxies (ES/S0). This is seen in Figure 5, in which the $M_{\text{bh}}-M_{*,\text{gal}}$ relation for the E galaxies is basically²² the same as the $M_{\text{bh}}-M_{*,\text{sph}}$ relation for the E galaxies. The $M_{\text{bh}}-M_{*,\text{gal}}$ relation for the E galaxies is, however, offset from the $M_{\text{bh}}-M_{*,\text{sph}}$ relation for the ES/S0 galaxies. The darker shading in this diagram reveals that the relations are not consistent with each other at the 1σ level. This reveals that the E and ES/S0 galaxies are not offset from each other in the $M_{\text{bh}}-M_{*,\text{sph}}$ diagram due to the exclusion of the non-spheroid stellar mass.

In Figure 6, we present the $(M_{\text{bh}}/M_{*,\text{gal}})-M_{*,\text{gal}}$ diagram. As noted in Sahu et al. (2019a), one can *approximate* the ETGs (E/ES/S0) with a single relation in this diagram if, for example, one is pursuing rough predictions for black hole masses in other ETGs. However, there is more detail to it than this, and this detail is one of the keys to understanding the black hole mass scaling diagrams.

As with Figure 2, one can again see that the addition of the non-spheroid stellar mass, primarily from the disc and bar, does not align the lenticular and elliptical galaxies. This reveals that the offset in the $M_{\text{bh}}-M_{*,\text{sph}}$ diagram, between the bulge component of ES/S0 galaxies and E galaxies, is not an artifact of separating/reducing the light in some ETGs (those with discs) but not others (those without) when we were plotting the spheroid stellar mass. The arrows in Figure 6 reveal that the distribution of elliptical galaxies is readily explained if they are built from the dry merger of lenticular galaxies, which is widely thought to be the case, and also the merger of elliptical galaxies.²³ However, what is not well-recognised is the ensuing offset between the E and ES/S0 galaxies in various black hole mass scaling diagrams populated with real data. Here, we have:

- built on Sahu et al. (2019a) which established that there is not a single (fundamental) $M_{\text{bh}}-M_{*,\text{sph}}$ relation for ETGs;
- revealed that mergers have not built a near-linear $M_{\text{bh}}-M_{*,\text{sph}}$ relation, due to the folding-in of the disc/bar stellar mass, reducing the $M_{\text{bh}}-M_{*,\text{sph}}$ ratio; and
- established that a single $M_{\text{bh}}-M_{*,\text{gal}}$ relation is not a fundamental relation for ETGs, with merger-built E galaxies offset from the S0 galaxies.

We will return to these points with additional supportive evidence in Section 3.3.

3.2 The $M_{\text{bh}}-M_{*,\text{sph}}$ and $M_{\text{bh}}-M_{*,\text{gal}}$ relations and ratios

We have used hierarchical Bayesian model fitting through the state-of-the-art platform for statistical modelling known as STAN (Carpenter et al. 2017; Team 2016)²⁴. The statistical model used for our linear regression considered uncertainties in both variables and is aimed at obtaining a symmetric relation between the two variables. A bivariate normal density was used to represent the distribution of latent (‘true’) $\log M_*$ and $\log M_{\text{bh}}$ values that might occur in our sample. As noted in Davis et al. (2019), “this is conceptually equivalent to the generative framework sketched by Hogg et al. (2010),

²² Nuclear discs and additional, possibly undigested, galaxy components result in a slight difference.

²³ While we have used simple equal-mass mergers to illustrate S0-to-E, and E-to-E, transformations, there are other options, such as several minor mergers.

²⁴ <https://mc-stan.org/>

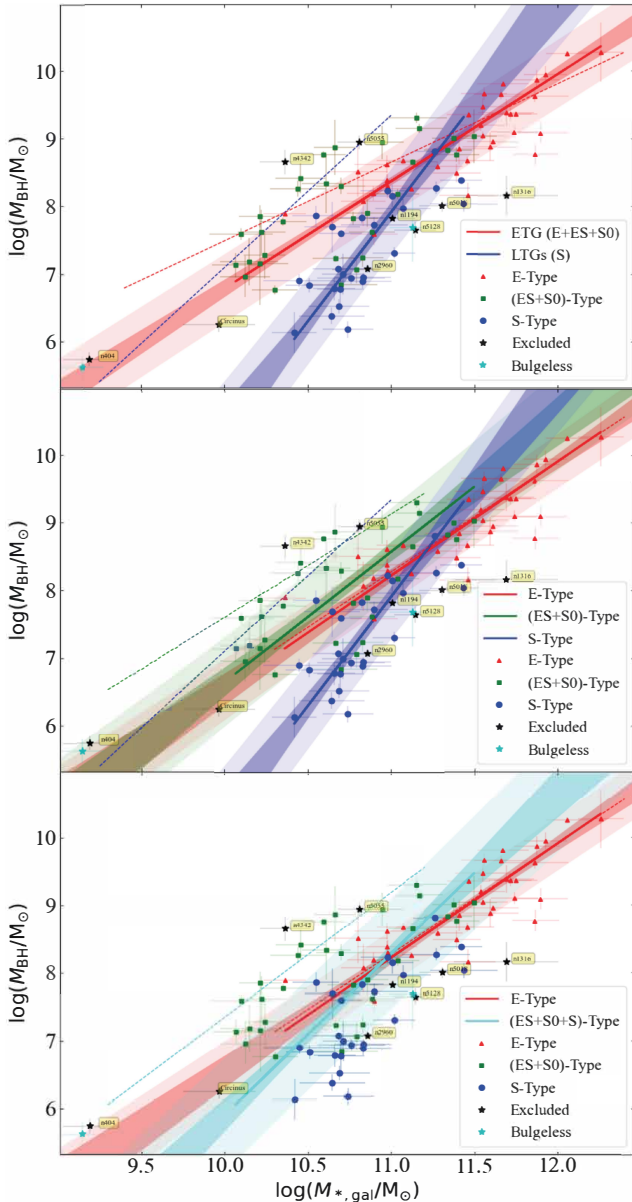


Figure 5. Similar to Figure 2 but now showing the *galaxy's* stellar mass, obtained via Equation 4, rather than the *spheroid's* stellar mass. The faint dashed lines are the $M_{\text{bh}}-M_{*,\text{sph}}$ relations from Figure 2. The bulgeless galaxy NGC 4395, with a rather blue $B-V$ colour of 0.445, and thus low $M_*/L_{3.6}$ ratio, can be seen in the lower left next to NGC 404.

in which the observed data points are imagined to be drawn from a distribution centred around a ‘line of best fit’, except that here we allow Bayesian ‘shrinkage’ by estimating the underlying distribution along the line rather than keeping this as an improper uniform prior.” Details of the statistical model framework are described in Davis et al. (2019, their Appendix A).

The best-fitting relations are shown in Table 2, along with the slope, A , and intercept, B , at the normalisation point. The normalisation point of, for example, the $M_{\text{bh}}-M_{*,\text{sph}}$ relation is $\nu(5 \times 10^{10} M_{\odot})$. If using equation 4 to convert light into stellar mass and thus derive a value of $M_{*,\text{sph}}$ for use in the $M_{\text{bh}}-M_{*,\text{sph}}$ equation (to predict M_{bh}), one has that $\nu = 1$. If, however, a different light-to-mass ratio prescription is preferred and used to derive

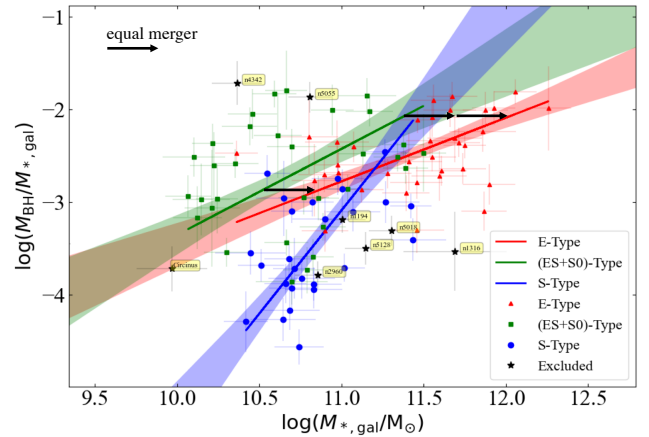


Figure 6. Similar to Figure 3 but now showing the $M_{\text{bh}}/M_{*,\text{gal}}$ mass ratio versus $M_{*,\text{gal}}$. The lines from the middle panel of Figure 5 have been mapped here. On average, the low-mass E galaxies have roughly the same $M_{\text{bh}}/M_{*,\text{gal}}$ ratio as the S0 galaxies which merged to create them, but twice as much stellar mass, in accord with a likely dry equal-mass merger. The high-mass E galaxies, including some brightest cluster galaxies, have four times as much mass as the S0s with a similar $M_{\text{bh}}/M_{*,\text{gal}}$ ratio, reflective of two such mergers or equally one equal-mass E galaxy merger.

one’s estimate of $M_{*,\text{sph}}$, then one needs to apply the appropriate value of ν , as illustrated in Sahu et al. (2019a, see their Figure 4 and Equations 6 to 8) for colour-dependent light-to-mass ratio prescriptions in different passbands. While we could drop this ν term from our equations, as typically done before Davis et al. (2019, see their Equations 10 and 11), its inclusion serves to remind readers that a specific prescription for Υ_* has been used to derive the equation and that they need to apply a conversion if using an alternate prescription. The root mean square scatter, Δ_{rms} , in the $\log M_{\text{bh}}$ direction is also tabulated for reference, although it is noted that this is not the quantity that is minimised with a Bayesian regression.

We have also applied three additional linear regression codes to our data, and found consistent results with our primary Bayesian analysis. For example, the Bisector regression from the Bivariate Correlated Errors and Intrinsic Scatter (BCES) routine (Akritas & Bershady 1996) gave the following slopes in the $M_{\text{bh}}-M_{*,\text{sph}}$ diagram for the E, ES/S0, and S galaxies: 1.62 ± 0.17 ; 1.49 ± 0.13 ; and 2.19 ± 0.33 . Using a symmetrical treatment²⁵ of the modified-FITEXY routine from Tremaine et al. (2002) yielded slopes equal to 1.65 ± 0.12 , 1.53 ± 0.11 and 2.20 ± 0.26 , respectively. Finally, the Bayesian LINMIX code from Kelly (2007) yielded: 1.61 ± 0.14 (E); 1.52 ± 0.13 (ES/S0); and 2.14 ± 0.34 (S). From Table 2, we have that $M_{\text{bh}} \propto M_{*,\text{sph}}^{2.25 \pm 0.39}$ for the bulges of the spiral galaxies. This has 1σ uncertainties which overlap with those from the steeper relation reported by Davis et al. (2019), in which $M_{\text{bh}} \propto M_{*,\text{sph}}^{2.44 \pm 0.33}$ for a larger sample of 40 spiral galaxies observed with a range of filters and M_*/L ratios. It appears that the bulges of spiral galaxies define a steeper $M_{\text{bh}}-M_{*,\text{sph}}$ relation than the bulges of S0 galaxies. Three evolutionary pathways for the spiral galaxy bulges are offered in

²⁵ While the modified-FITEXY routine performs a non-symmetrical regression of a sample of (X, Y) data pairs, a symmetrical treatment can be obtained by running the regression twice, the second time with the Y and X variables swapped around with each other. The *bisector* of the resulting two regression lines provides an expression which effectively treats the data equally (e.g., Novak et al. 2006; Graham & Driver 2007b, their Section 3.1.1).

Section 4. In fair agreement with the relations found here for the ETGs using the hierarchical Bayesian model fitting (see Table 2), Sahu et al. (2019a) report a slope of 1.86 ± 0.20 for 36 ES/S0 galaxies and 1.90 ± 0.20 for 40 E galaxies. As seen in Sahu et al. (2019a), the present sample of E galaxies trace a relation which is roughly parallel to that defined by the bulges of S0 galaxies.

Using multicomponent decompositions, Savorgnan et al. (2016) reported a median $M_{\text{bh}}/M_{*,\text{sph}}$ value of ~ 0.68 percent for 45 ETGs, which they thought followed a near-linear $M_{\text{bh}}-M_{*,\text{sph}}$ relation. This result was based on the use of an $M_*/L_{3.6}$ ratio of ~ 0.60 and a Chabrier (2003) IMF. Bernardi et al. (2010) suggest a reduction of just 0.05 dex to the logarithm of Y_* ($\equiv M_*/L$) to convert from the Chabrier (2003) IMF to the Kroupa (2002) IMF. Therefore, this $M_{\text{bh}}/M_{*,\text{sph}}$ mass ratio of 0.68 percent increases to 0.76 percent for the Kroupa (2002) IMF. This is comparable to the median $M_{\text{bh}}/M_{*,\text{sph}}$ ratio for core-Sérsic galaxies reported in Graham & Scott (2013), which was obtained using $M_*/L_K = 0.8$ from Bell et al. (2003) and based on a diet-Salpeter IMF. Their reported K -band mass-to-light ratio of 0.49 drops by 0.15 dex, or to $M_*/L_K = 0.57$, when switching to the Kroupa (2002) IMF. Consequently, their $M_{\text{bh}}/M_{*,\text{sph}}$ ratio of 0.49 percent increases to 0.69 percent once calibrated against the Kroupa (2002) IMF, and is thus in good agreement with the above value of 0.76 percent.²⁶ However, as Sahu et al. (2019a) uncovered, and as can be seen in Figure 3, this near-constant $M_{\text{bh}}/M_{*,\text{sph}}$ mass ratio of ~ 0.7 percent for ETGs is misleading. Individual ratios, at a fixed $M_{*,\text{sph}}$, differ by an order of magnitude depending on whether the system is an S0 or an E galaxy. Furthermore, the ratio can vary by an order of magnitude within either of these two galaxy types. Turning to the galaxy masses, Figure 6 illustrates that while the S galaxies tend to have lower $M_{\text{bh}}/M_{*,\text{gal}}$ ratios than the ETGs in our sample, due in part to the greater disc-to-bulge ratios in S galaxies, there is more to it than that. On average, for a given $M_{\text{bh}}/M_{*,\text{gal}}$ ratio, the E galaxies have higher masses than the S0 galaxies, which is expected if S0 galaxies merge to form E galaxies. This observation also expresses itself as a lower $M_{\text{bh}}/M_{*,\text{gal}}$ ratio in E galaxies than S0 galaxies at a given galaxy mass, modulo the scarcity of low-mass E and high-mass S0 galaxies — another signature of the dry merger phenomena.

In passing we note that it almost goes without saying that applying consistent Y_* ratios between different studies is vital for avoiding artificial mismatches such as that reported in Shankar et al. (2016). Realised some years ago, and detailed in (Sahu et al. 2022b), this mismatch led us to introduce the mass-to-light conversion term, ν , in Davis et al. (2019).²⁷ This was developed further in Sahu et al. (2019a) and explains the ν term included in Table 2.

Here, we find $M_{\text{bh}}/M_{*,\text{sph}} = 0.0018$ (0.18 percent) for elliptical galaxies with $M_{*,\text{sph}} = 10^{11} M_\odot$, and 1.7 percent for bulges of the same stellar mass. The order of magnitude difference between these morphological types can be seen in Figure 3. This difference appears to widen slightly when moving to lower spheroid masses. Furthermore, one can see how dry mergers of S0 galaxies, building E galaxies, can explain this observation.

²⁶ We thank Peter Behroozi for pointing out this issue in 2017, surrounding clarification of the adopted IMF before comparing $M_{\text{bh}}/M_{*,\text{sph}}$.

²⁷ The lower-case epsilon symbol was introduced to facilitate changes to the mass-to-light ratio, Y , in a similar manner to how h can enact changes to the adopted Hubble-Lemaître constant H_0 .

Table 2. Black hole mass scaling relations

Galaxy type	Slope (A)	Intercept (B)	Δ_{rms}
$\log(M_{\text{bh}}/M_\odot) = A \log[M_{*,\text{sph}}/\nu(5 \times 10^{10} M_\odot)] + B$			
E (35)	1.64 ± 0.17	7.79 ± 0.17	0.38
ES/S0 (32)	1.53 ± 0.15	8.67 ± 0.15	0.44
S (26)	2.25 ± 0.39	8.66 ± 0.28	0.57
ES/S0 & S (58)	1.84 ± 0.16	8.63 ± 0.14	0.55
E & ES/S0 (67)	1.16 ± 0.07	8.30 ± 0.11	0.43
$\log(M_{\text{bh}}/M_\odot) = A \log[M_{*,\text{gal}}/\nu 10^{11} M_\odot] + B$			
E (35)	1.69 ± 0.17	8.22 ± 0.15	0.38
ES/S0 (32)	1.93 ± 0.28	8.57 ± 0.17	0.61
S (26)	3.23 ± 0.57	7.91 ± 0.18	0.60
ES/S0 & S (58)	2.38 ± 0.27	8.28 ± 0.13	0.80
E & ES/S0 (67)	1.59 ± 0.11	8.37 ± 0.11	0.49
$\log(M_{\text{bh}}/M_\odot) = A \{\log[M_{*,\text{sph}}/M_{*,\text{gal}}] - (-0.5)\} + B$			
ES/S0 (31)	4.00 ± 0.58	7.71 ± 0.16	0.64
S (26)	3.23 ± 0.63	7.99 ± 0.21	0.78
$\log(M_{\text{sph}}/\nu M_\odot) = A \log[R_{\text{e},\text{sph},\text{eq}}/\text{kpc}] + B$			
All (93)	1.14 ± 0.04	10.48 ± 0.08	0.29
$\log(M_{\text{bh}}/M_\odot) = A \log[R_{\text{e},\text{sph},\text{eq}}/\text{kpc}] + B$			
E (35)	2.38 ± 0.33	6.88 ± 0.32	0.58
ES/S0 (32)	1.98 ± 0.24	8.52 ± 0.16	0.54
S (26)	2.40 ± 0.40	8.02 ± 0.20	0.65

The slope and intercept of the relations shown in Figures 2, 4, 5, 7 and 8 have been obtained using a Bayesian analysis that treats the data symmetrically. The root mean square (rms) scatter reported here, Δ_{rms} , is the vertical scatter about each relation. The spheroid and galaxy stellar masses have been obtained using the M_*/L prescription given in Equation 4. The ν term is mentioned towards the end of Section 3.2 is equal to 1 if one uses stellar masses consistent with those obtained via Equation 4.

3.3 From bulges to elliptical galaxies

Much of the accretion-driven growth of black holes is known to occur in regular star-forming disc galaxies (e.g., Gabor et al. 2009; Cisternas et al. 2011). That is, the AGNs tend to reside in normal, often isolated, spiral galaxies (e.g., Grogin et al. 2005; Kocevski et al. 2012). AGNs are not particularly prevalent during or after major mergers. Given that elliptical galaxies have little to no star formation, it is apparent that the gaseous processes driving growth in the $M_{\text{bh}}-M_{*,\text{sph}}$ diagram occur in bulges. As noted by multiple studies, the black hole accretion rate relative to the star formation rate is such that it is not expected to establish a linear $M_{\text{bh}}-M_{*,\text{gal}}$ relation but instead a steeper relation (e.g., Seymour et al. 2012; LaMassa et al. 2013; Drouart et al. 2014; Delvecchio et al. 2019). This bodes well for the steeper-than-linear trend seen for spiral galaxies in the $M_{\text{bh}}-M_{*,\text{gal}}$ diagram. Should some of the star-formation be occurring in bulges, then the higher (black hole accretion rates)-to-(star-formation rates) in spiral galaxies may mesh well with the trend seen in the $M_{\text{bh}}-M_{*,\text{sph}}$ diagram.

By considering the sizes of the spheroids, we can build a more informed scenario for what we are witnessing in the $M_{\text{bh}}-M_{*,\text{sph}}$ and $M_{\text{bh}}-M_{*,\text{gal}}$ diagrams. We will see how dry mergers can account for the steeper-than-linear $M_{\text{bh}}-M_{*,\text{sph}}$ relation observed for the E galaxies.

In Figure 7, we show the effective half-light size of the spheroids, $R_{\text{e},\text{sph}}$, versus their stellar mass, $M_{*,\text{sph}}$. These radii are given in Table 1, along with the reference showing the modelled light profile from which the radii were measured. We used the

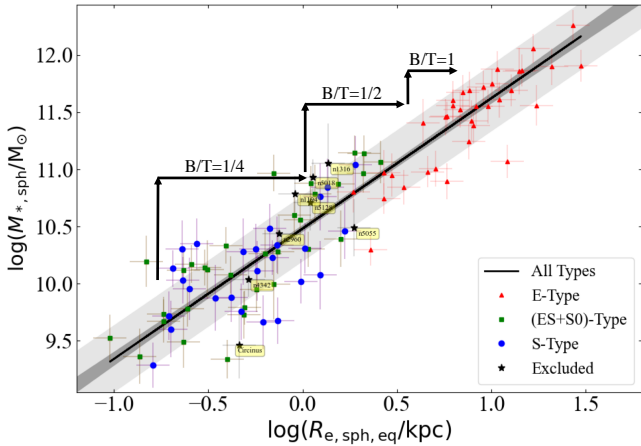


Figure 7. Geometric-mean axis, aka ‘equivalent (circular) axis’, effective half-light radii, $R_{e,sph,eq}$, of the spheroid versus the stellar mass of the spheroid, $M_{*,sph}$. Modification of Sahu et al. (2020), their Figure 9) using the stellar mass-to-light prescriptions in Equation 4 and only those galaxies with $3.6\ \mu\text{m}$ data. The arrows show the apparent movement caused by creating an E galaxy from an equal-mass dry merger between two S0 galaxies with bulge-to-total ratios equal to one-quarter and one-half and between two elliptical galaxies with $B/T = 1$. The length of the horizontal arrows are based on maintaining the observed relation $M_{*,sph} \propto R_{e,sph,eq}^{1.14 \pm 0.04}$. The E galaxies with the larger radii at $\log(M_{*,sph}/M_{\odot}) \approx 10.25$ and 11.05 are NGC 3377 and NGC 4697, respectively.

geometric-mean axis, aka the ‘equivalent axis’, $r = \sqrt{ab}$, along which the size of the radii are equivalent to a circularised version of the quasi-elliptical isophotes. There is no discontinuity in the $R_{e,sph}-M_{*,sph}$ diagram between the different types of spheroids. This continuity holds whether the spheroids coexist with a disc that either does or does not contain a spiral pattern, or whether they exist on their own with no disc, i.e., are an elliptical galaxy.

The $R_{e,sph}-M_{*,sph}$, or equally $M_{*,sph}-R_{e,sph}$, relation is seen in Figure 7 to have a slope close to unity. Curiously, there is little evidence for any broad curvature in the distribution of $R_{e,sph}$ and $M_{*,sph}$. This differs from what is seen in the $M_{*,gal}-R_{e,gal}$ relation for ETGs (Graham et al. 2006, their Figure 1b) due to the presence and then dominance of discs as one moves to lower masses. Not surprisingly, this near-linear slope matches that seen at the bright end of the $M_{*,gal}-R_{e,gal}$ relation for ETGs, which is dominated by E galaxies (e.g., Graham & Worley 2008; Krajnović et al. 2018; Dullo 2019; Sahu et al. 2020, their Figure 9), i.e., systems without discs. The simulations from Nipoti et al. (2009a), involving elliptical galaxies undergoing minor and major dry merger events, build a near-linear $M_{*,gal}-R_{e,gal}$ relation (Nipoti et al. 2009b). This relation will be explored further in Hon et al. (2022b) with a sample twice that used here and having multicomponent decompositions and a consistent set of Y_* ratios.

In the left-hand panel of Figure 8, we see the black hole masses versus the half-light radii of the host spheroids, as measured from the geometric-mean axis. Given the strong relation between the sizes and the masses of the spheroids seen in Figure 7, it is not too surprising that the structure in the $M_{bh}-R_{e,sph}$ diagram (Figure 8) shows a similarity to that seen in the $M_{bh}-M_{*,sph}$ diagram (Figure 2). Using the $M_{*,sph}-R_{e,sph}$ diagram (Figure 7), one can map the expected shift in the $M_{bh}-M_{*,sph}$ diagram for equal-mass mergers of S0 galaxies that produce an E galaxy. This is shown in the right-hand panel of Figure 8, and can be understood in terms of the

galaxies effectively folding in their disc stars to make the new E galaxy and thereby lowering the $M_{bh}/M_{*,sph}$ ratio, as seen in Figure 3. This scenario also readily explains the offset between bulges and E galaxies seen in Figure 8. For example, a merger of two equal-mass S0 galaxies with $B/T=0.25$ (e.g., Laurikainen et al. 2005; Graham & Worley 2008) will double M_{bh} and increase the spheroid (now elliptical galaxy) mass 8-fold once the disc light is incorporated. In the $M_{bh}-M_{*,sph}$ diagram, this merger moves a high stellar mass S0 up by 0.3 dex and across by 0.9 dex, placing it on the sequence of elliptical galaxies. From the relation $M_{*,sph} \propto R_{e,sph,eq}^{1.14 \pm 0.04}$ (based on the Spitzer sample used here), we have that a 0.9 dex increase in $M_{*,sph}$ is associated with a 0.79 dex increase in $R_{e,sph,eq}$. Such an increase from a major merger event is plotted in Figures 7 and 8. Figure 8 provides a previously unstated measure-of-sorts of the average number of major mergers the E galaxies in our sample have experienced. There is evidence here, and in Figure 6, that BCGs have experienced a greater number of mergers, and this will be explored in more detail in a subsequent paper.

4 DISCUSSION

4.1 Overmassive and undermassive black holes

Early observational bias favouring the detection of systems with big black holes led to samples dominated by elliptical galaxies and lenticular galaxies with massive bulges. This sample selection produced an apparent near-linear $M_{bh}-M_{*,sph}$ relation, which steepened as lower-mass black holes were gradually included. Figure 9 reveals how this near-linear ‘red sequence’ in the $M_{bh}-M_{*,sph}$ diagram arises by sampling both massive bulges and elliptical galaxies. For many such elliptical galaxies, their spheroid mass may be dominated by the disc masses of their progenitor galaxies. This explains the approximately order of magnitude lower $M_{bh}/M_{*,sph}$ ratio in elliptical galaxies when compared to bulges of the same ‘spheroid’ mass (Figure 3). As noted earlier, this is not because the galaxies’ disc masses are excluded from the $M_{bh}-M_{*,sph}$ diagram; the $M_{bh}/M_{*,gal}$ ratio is not equal among ES/S0 and E galaxies at a given galaxy stellar-mass (Figure 6).

The notion of a ‘red sequence’ representing the underlying fundamental connection between black holes and ‘classical bulges’, i.e., bulges built by mergers, introduces problems that disappear when considering the $M_{bh}-M_{*,sph}$ diagram in terms of a bulge sequence and an offset merger-built population of elliptical galaxies. Most obvious is that the E galaxies do not follow the (near-linear) red sequence but define a steeper non-linear relation (see Table 2). In addition, the low- and high-mass bulges appear as outliers from the near-linear ‘red sequence’, invoking a misleading perception as to the need for separate formation physics. It had led to the notion that massive bulges and relic galaxies are a disconnected population with overmassive black holes relative to galaxies on the near-linear relation (see Figure 9). They are, however, not overmassive relative to the bulge sequence. Furthermore, while some black holes in BCGs appear overmassive relative to the ‘red sequence’, they are not overmassive relative to the elliptical galaxy $M_{bh}-M_{*,sph}$ sequence. By appreciating the role of mergers, we can understand how the morphology-dependent relationships arose in the $M_{bh}-M_{*,sph}$ and $M_{bh}-M_{*,gal}$ diagrams. The near-linear red-sequence also resulted in claims that low-mass bulges were yet another disconnected population with undermassive black holes relative to galaxies on the red-sequence. However, they are not undermassive relative to the bulge sequence. We again note that while our sample

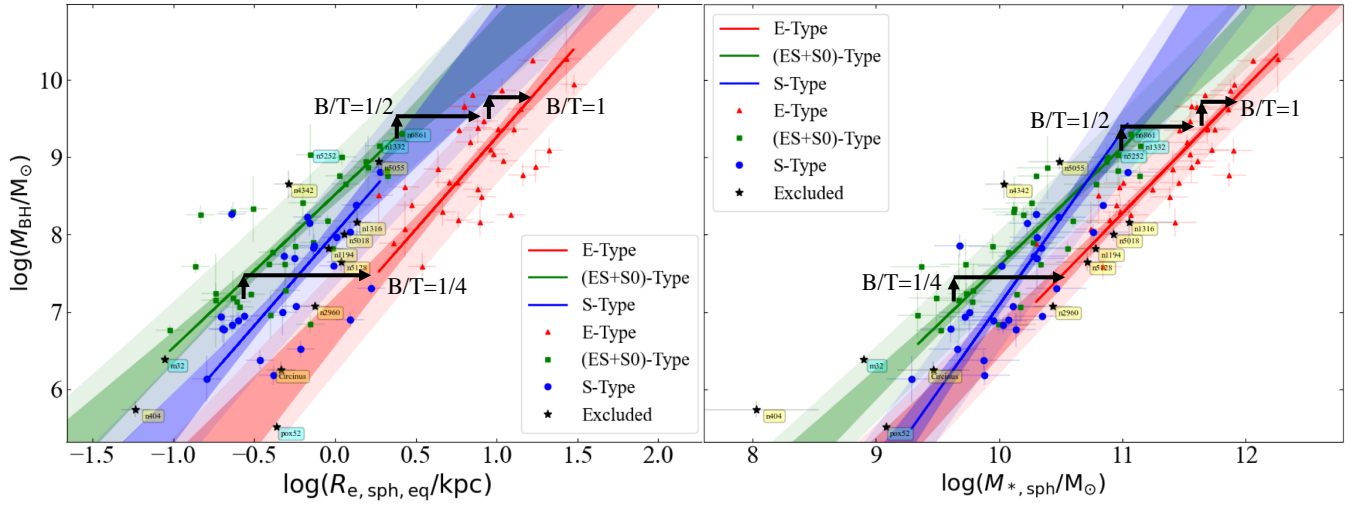


Figure 8. Left-hand panel: M_{bh} versus $R_{\text{e},\text{sph},\text{eq}}$. Adaption of Figure 13 from [Sahu et al. \(2020\)](#), using only those galaxies with $3.6\ \mu\text{m}$ data and updated values reported in Table 1. Right-hand panel: Evolution in the $M_{\text{bh}}-M_{*,\text{sph}}$ diagram arising from dry equal-mass mergers of galaxies with bulge-to-total (B/T) ratios of 1.0, 0.5 and 0.25 to produce an E galaxy. The E galaxy sequence is seen to follow a steeper-than-linear relation rather than the linear relation expected from E+E galaxy mergers ([Peng 2007](#)). The somewhat discrepant (low $M_{*,\text{sph}}$ or high M_{bh}) spiral and elliptical galaxy with $\log(M_{\text{bh}}/M_{\odot}) \approx 7.9$ dex are NGC 1300 and NGC 3377, respectively.

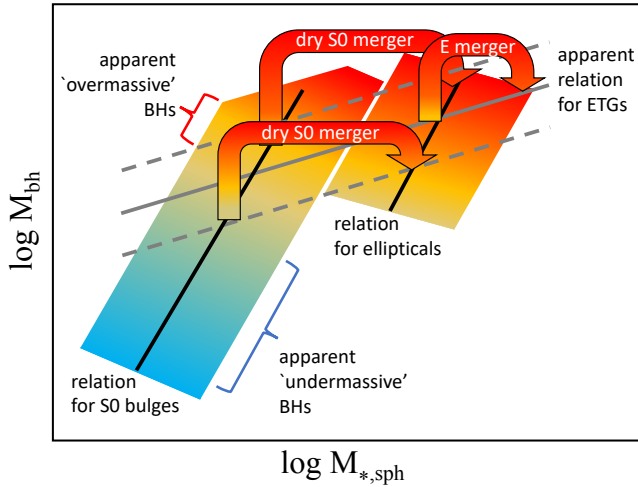


Figure 9. Schematic of the $M_{\text{bh}}-M_{*,\text{sph}}$ diagram for ETGs. The steep band on the left shows a relation for bulges (in S0 and ES galaxies). The steeper band on the right shows the relation for E galaxies. The shallower relation, shown in grey, tracks an apparent ‘red sequence’ obtained by sampling some massive bulges and some elliptical galaxies. Past claims for apparently overmassive and undermassive black holes, relative to this near-linear ‘red sequence’, can be understood in terms of the host bulge belonging to the (steeper) bulge sequence.

of bulges does contain members which reside below the ‘red sequence’, they are not the (peanut shell)-shaped structures associated with unstable bars, nor are they nuclear or inner discs which we model with separate components.

4.1.1 Relic red nuggets at the top of the bulge sequence

The gaseous processes that gave rise to some bulges may have occurred long ago. Indeed, many local bulges could be the descendants of the ‘red nuggets’ observed at $z \approx 2.5 \pm 1$ ([Daddi et al. 2005](#); [Damjanov et al. 2011](#)) and potentially now cloaked in a large-scale disc ([Graham et al. 2015](#); [de la Rosa et al. 2016](#); [Hon et al. 2022a](#), and references therein). If any of the high- z red nuggets did not acquire a disc by today—which may be likely if they started life in a proto-(galaxy cluster), given (i) the propensity for ram-pressure stripping of cold gas by hot gas, and (ii) the reduction in galaxy mergers due to high fly-by speeds—, then they will remain a compact massive galaxy today (e.g., [Zwicky 1966](#); [Zwicky & Kowal 1968](#); [Zwicky & Zwicky 1971](#); [Saracco et al. 2010](#); [Valentinuzzi et al. 2010](#); [Poggianti et al. 2013](#); [Trujillo et al. 2014](#)). Such local ‘compact galaxies’ are also referred to as ‘relic galaxies’ if their stars are old (e.g., [Ferré-Mateu et al. 2017](#)). In separating spheroidal types, the ‘relic galaxies’ are seen not to be associated with the merger-built E galaxies in the $M_{\text{bh}}-M_{*,\text{sph}}$ diagram but rather sit on the bulge sequence, with the most massive red relics located at the top. Consequently, Figure 9 reveals how massive relic galaxies appear to have overmassive black holes relative to the near-linear ‘red sequence’ but are consistent with the bulge sequence for ETGs.

NGC 1332 is not an elliptical galaxy but a relic ES galaxy which has not acquired/built a large-scale disc. The dominant spheroidal component in NGC 1332 has $\log(M_{*,\text{sph}}/M_{\odot}) = 11.15 \pm 0.15$ dex and a geometric mean radius $R_{\text{e},\text{sph}} \approx 1.9$ kpc. It has the second highest black hole mass of the ES+S0 galaxies in our sample, and can be seen to reside at the top of the bulge sequence in Figure 8. We have also labelled the ES galaxy NGC 6861 in Figure 8, which has $\log(M_{*,\text{sph}}/M_{\odot}) = 11.07 \pm 0.19$ and $R_{\text{e},\text{sph}} \approx 2.6$ kpc.

If a high- z ‘red nugget’ acquired a disc over time, then today the ‘red nugget’ would be the compact massive spheroid of a disc galaxy. NGC 5252, for example, likely has such a relic bulge ([Sahu et al. 2019a](#)); and also a relic quasar ([Capetti et al. 2005](#)). Given the old ages of discs in massive lenticular galaxies, the bulk of their

stars formed long ago, no doubt acquired through direct accretion and mergers but also possibly via star-formation in their gas discs at cosmic noon (e.g., [Florez et al. 2020](#)).

4.1.2 Merger-built Brightest Cluster Galaxies

The creation of BCGs via (multiple) mergers produces the largest elliptical galaxies, found at the centres of galaxy groups and clusters. The steeper-than-linear $M_{\text{bh}} \propto M_{*,\text{sph}}^{1.72}$ relation seen in [Bogdán et al. \(2018, their Figure 3\)](#) for BCGs is explained here as a combination of mergers folding in the disc mass and a steep origin relation for the bulges of the pre-merged progenitor galaxies in the $M_{\text{bh}}-M_{*,\text{sph}}$ diagram. That is, the elliptical galaxies, which include the BCGs²⁸, should not be thought of as a departure from a near-linear $M_{\text{bh}}-M_{*,\text{sph}}$ relation. Instead, they represent a shift to a somewhat parallel relation to that defined by the bulges of ETGs. Of course, when E+E dry mergers build new E galaxies, the evolutionary path in the $M_{\text{bh}}-M_{*,\text{sph}}$ diagram will be along a vector with a slope of 1. One might imagine that in the Universe’s distant future, one would start to see a linear relation for BCGs emerge from the top end of the current relation for the E galaxies. This is, however, something which we will leave for the simulators.

4.2 The stripped S0 galaxy M32

In Figure 7, M32 appears to the left of the $M_{\text{bh}}-M_{*,\text{sph}}$ relation defined by bulges in ETGs. However, it resides within the 1σ scatter about this relation. The slight preference to the left may reflect that the bulge, along with the disc, in M32 has been eroded by its massive neighbour, M31. This process can reduce the bulge mass and inflate its half-light radius. ‘Compact elliptical’ (cE) galaxies like M32, which have lost the gravitational tug-of-war to retain ownership of their stars ([Roche 1850](#); [Toomre & Toomre 1972](#)), stand out in the galaxy colour-magnitude diagram due to their low luminosity for their colour (e.g., [Graham & Soria 2019, their Figure 11](#)). For M32, the $V - I$ (Vega) colour of $\sim 1.2-1.4$ mag ([Lauer et al. 1998](#)) implies $M_*/L_I \approx 3M_{\odot}/L_{\odot}$ ([Schombert et al. 2022](#)), or ~ 2.4 after converting to a [Kroupa \(2002\)](#) IMF. Coupled with 0.09 mag of Galactic extinction, the absolute magnitude for the spheroidal component of M32, $M_I = -17.0$ mag (Vega: [Graham & Spitler 2009](#)), corresponds to $M_* \approx 0.8 \times 10^9 M_{\odot}$. Performing a multi-component fit to M32’s major-axis light profile, [Graham & Spitler \(2009\)](#) measured an effective half light-radius of $26''.3$ for the bulge component. For an ellipticity of 0.3 at this radius, this translates to an equivalent-axis $R_{\text{e},\text{sph},\text{eq}} = 22''$. Using a scale of 4 pc per $1''$, this angular size is equal to a physical size of 88 pc, as shown in Figure 8.

We add the dwarf E galaxy Pox 52 (93 Mpc distant), with $M_{\text{bh}} = (3.2 \pm 1) \times 10^5 M_{\odot}$ and $M_{*,\text{sph}} = 1.2 \times 10^9 M_{\odot}$. We use $R_{\text{e},\text{eq}} = 436$ pc ([Thornton et al. 2008](#)), based on a minor-to-major axis ratio $b/a = 0.79$ ([Barth et al. 2004](#)) and $R_{\text{e},\text{maj}} = 490$ pc ([Thornton et al. 2008](#)). Pox 52 follows both the $M_{\text{bh}}-M_{*,\text{sph}}$ and $M_{\text{bh}}-R_{\text{e},\text{sph}}$ relations well.

There is another spheroid in our sample, albeit not used in our regression analyses, with a smaller mass and size than that of

M32. The dwarf S0 galaxy NGC 404 can be seen in Figure 8 to follow the S0 galaxy sequence in the $M_{\text{bh}}-R_{\text{e},\text{sph}}$ diagram but reside to the left of the S0 galaxy sequence in the $M_{\text{bh}}-M_{*,\text{sph}}$ diagram. This LINER galaxy has a bright ($r \approx 2''$) nuclear spiral pattern (compare CG 611: [Graham et al. 2017](#)) and is encircled by a much larger H I gas disc with knotty, irregular tendrils of UV hotspots and H II regions ([Williams et al. 2010](#); [Bresolin 2013](#)). However, this galaxy is excluded from the fitting process because its location at the lower extremum of our data might excessively torque the fitted relation. This becomes problematic using such a datum if its measurements are in error or if the scaling relation does not extend linearly to such low black hole masses. [Nguyen et al. \(2017\)](#) reported a 3σ upper limit to the black hole mass of $1.5 \times 10^4 M_{\odot}$, which was recently revised to $M_{\text{bh}} = 5.5^{+4.1}_{-3.8} \times 10^5 M_{\odot}$ ([Davis et al. 2020](#)). In passing, we note how this discrepancy highlights the affect of systematic errors not captured by the small formal/random errors typically reported for most black hole mass measurements. We also attach a 0.5 dex uncertainty to our spheroid mass, which may be three times less massive than our adopted value from [Sahu et al. \(2019a\)](#) if this galaxy has an anti-truncated disc ([Graham & Sahu 2022](#)), resulting in a steeper inner-disc component at the expense of the bulge.

LEDA 87000 is a galaxy that likely harbours a central intermediate-mass black hole ([Baldassare et al. 2015](#)). Although [Graham et al. \(2016a\)](#) observed it to follow the near-quadratic $M_{\text{bh}}-M_{*,\text{sph}}$ relation followed by LTGs, inspection of subsequent Hubble Space Telescope images reveals that the previously poorly-resolved ‘barge’ component²⁹ — as seen in ground-based images — was all bar and no bulge ([Baldassare et al. 2017](#)). This represents something of a growing trend in which the closer one looks, the more ‘bulges’ — when simply defined as the excess of light above the inward extrapolation of an outer exponential disc — retreat by giving up ground to bars or other features (e.g., [Balcels et al. 2003](#); [Erwin et al. 2003](#); [Laurikainen et al. 2005](#); [Hon et al. 2022a](#)).

4.3 The primary relation

The larger, merger-built elliptical galaxies are seen to define a secondary, or at least subsequent, relation in the $M_{\text{bh}}-M_{*,\text{sph}}$ diagram. In terms of Darwinian evolution on a galaxy scale, they can be thought of as coming into existence via punctuated equilibrium rather than gradualism. Major dry mergers between S0 galaxies, in which the S0 galaxies effectively fold in all their disc stellar mass to create an elliptical galaxy, are accompanied by a substantial oversized jump in the stellar mass (relative to the jump in the black hole mass) and a large jump in the half-light size of the new spheroid, i.e., the elliptical galaxy. Such evolution explains the two prominent relations observed in the $M_{\text{bh}}-M_{*,\text{sph}}$ diagram and the $M_{\text{bh}}-R_{\text{e},\text{sph},\text{eq}}$ diagram for ETGs (Figure 8).

Broadly speaking, some bulges may have arisen from a kind of rapid monolithic collapse, or at least result from an early-formation process that created the observed high- z ‘red nuggets’, while most elliptical galaxies likely formed from a binary merger or hierarchical merging (in the case of the BCGs) over the age of the Universe. As such, a meaningful cosmological probe into the evolution of the galaxy/black hole scaling relations needs to be mindful of the galaxy morphology. For example, a sample of elliptical galaxies at $z = 1$ can not be directly compared with a sample of bulges at $z = 0$; to do so would be comparing apples and oranges.

To summarise, the notion of a single near-linear $M_{\text{bh}}-M_{*,\text{sph}}$

²⁸ Our galaxy stellar-masses are derived by excluding the surrounding ICL light, either because it was fit as a component during the galaxy decomposition and excluded here, or because the images and light profiles were not deep enough for the ICL to have been an issue.

²⁹ ‘Barge’ is an amalgamation of Bar+Bulge.

relation is inadequate and seems to offer misdirection in understanding galaxies and black holes. The averaging of black hole and galaxy masses through mergers has established neither the expected nor an observed near-linear $M_{\text{bh}}-M_{*,\text{sph}}$ relation. While we have presented the most accurate $M_{\text{bh}}-M_{*,\text{sph}}$ diagram to date, and interpreted the broad brush stroke near-parallel relations shown in Sahu et al. (2019a), there is further information to be gleaned from this diagram. Mergers, both wet and dry, which do not fold in all of the disc's stellar mass will be addressed in Graham & Sahu (2022), where we develop something of a phylogenetic tree diagram within the bivariate space of M_{bh} versus $M_{*,\text{sph}}$.

One should expect to observe morphology-dependent substructure in other black hole scaling diagrams. For example, as previously noted, the broad red/blue sequence for ETGs/LTGs in the $M_{\text{bh}}-M_{*,\text{gal}}$ diagram has been observed in the $M_{\text{bh}}-\text{colour}$ diagram (Dullo et al. 2020). This broad division may also appear in the $M_{\text{bh}}-\text{metallicity}$, Z , diagram (Warner et al. 2003; Kisaka et al. 2008). Depending how the number of globular clusters, N_{GC} , traces a galaxy's stellar mass (Mieske et al. 2014, and references therein), one may also expect the ETGs and LTGs to follow different trends in the $M_{\text{bh}}-N_{\text{GC}}$ diagram (Spitler & Forbes 2009; Burkert & Tremaine 2010). The number of red and blue globular clusters around each galaxy may yield yet further subdivisions (see Kundu & Whitmore 1998; Kuntschner et al. 2002), as may their kinematics (e.g., Sadoun & Colin 2012; Pota et al. 2013).

With our new understanding of the relevance of galaxy morphology and galaxy formation history, the role of mergers, and refined insight into what may be considered the primary relations versus their modified/evolved form, one is also better placed to tackle the question of whether or not a two-dimensional plane within a three-dimensional space may provide an improved description over bivariate linear relations. For example, does a third axis, in addition to M_{bh} and $M_{*,\text{sph}}$, uncover a distribution on a more fundamental plane? Our analysis, considering additional parameters obtained from physically-motivated multicomponent decomposition, such as the spheroid Sérsic index and stellar density (e.g., Graham & Driver 2007b; Saglia et al. 2016; Sahu et al. 2022a), along with spheroid size, mass, and velocity dispersion, will be presented in a forthcoming paper. Here, we restrict ourselves to briefly explaining why the combination of M_{bh} , $M_{*,\text{sph}}$, and $R_{\text{e},\text{sph},\text{eq}}$ (or equally³⁰ $\langle I \rangle_{\text{e}}$) may not produce a useful plane about which the scatter in the $\log(M_{\text{bh}})$ direction is less than that seen about the $M_{\text{bh}}-M_{*,\text{sph}}$ relation.

For the following thought experiment, we can consider two parallel relations in the $M_{\text{bh}}-M_{*,\text{sph}}$ diagram, one for S0 galaxy bulges and the other for an offset population of merger-built E galaxies. We can use the knowledge that the (logarithm of the) half-light spheroid radius scales with the (logarithm of the) spheroid stellar mass (Figure 7). One way to think of the problem is that we wish to introduce an $R_{\text{e},\text{sph},\text{eq}}$ term to effectively shift the E galaxies to the left in the $M_{\text{bh}}-M_{*,\text{sph}}$ diagram, to make them overlap with the bulges and thereby reduce the scatter seen in this diagram (see Figure 8). However, we need to bear in mind that this procedure will also shift the bulges to the left, given that we are assuming no knowledge of morphology and just using the parameters M_{bh} , $M_{*,\text{sph}}$, and $R_{\text{e},\text{sph},\text{eq}}$. It turns out that to achieve overlap of the elliptical and bulge samples, the necessary subtraction of a $\log R_{\text{e}}$

term from the $\log M_{*,\text{sph}}$ values in the $M_{\text{bh}}-M_{*,\text{sph}}$ diagram results in a near-vertical distribution of points with a near-infinite slope. Remember, $R_{\text{e},\text{sph},\text{eq}}$ scales almost linearly with $M_{*,\text{sph}}$. This shall be shown in a forthcoming paper but we felt it was of sufficient interest to provide some initial insight here.

4.4 Is there a role for AGN feedback in shaping the turnover and (high mass)-end of the galaxy mass function?

The observational results herein represent a considerable departure from the connection galaxies are often claimed or thought to have with their central black hole. More accurate spheroid masses — particularly from a greater awareness that many ETGs are S0s rather than Es — have revealed how the coevolution of *bulges* and supermassive black holes have built a super-linear³¹ or near-quadratic³² $M_{\text{bh}}-M_{*,\text{sph}}$ relation. Graham (2012) and Graham & Scott (2013) highlighted this steeper slope and discussed how dry mergers might be producing an offshoot of core-Sérsic galaxies, creating (what was thought to be) a near-linear slope at high black hole masses in the $M_{\text{bh}}-M_{*,\text{sph}}$ diagram. However, this idea did not account for the incoming disc mass during some mergers, or for the more recent observation that merger-built elliptical galaxies (with and without depleted cores) do not follow a near-linear $M_{\text{bh}}-M_{*,\text{sph}}$ relation. Obviously, AGN feedback has thus also not produced a near-linear $M_{\text{bh}}-M_{*,\text{sph}}$ relation for the elliptical galaxies. Moreover, the location of the elliptical galaxies in the $M_{\text{bh}}-M_{*,\text{sph}}$ diagram would appear to not be due to AGN feedback but rather major mergers in which the angular momenta of the progenitor galaxy's discs have largely cancelled. This observation is apparent from the $M_{\text{bh}}-M_{*,\text{sph}}$ diagram, the $M_{\text{bh}}/M_{*,\text{sph}}$ ratios (Figure 3), the $M_{\text{bh}}/M_{*,\text{gal}}$ ratios (Figure 6) and the $M_{\text{bh}}-R_{\text{e},\text{sph}}$ diagram (Figure 8).

While ‘quasar mode’ AGN feedback (discussed in Section 4.5) might contribute to a link between black hole mass and *bulge* mass for some lower mass systems, it is not yet well established how much it may regulate the gas and star formation in the discs of galaxies (e.g., Gabor & Bournaud 2014; Davis et al. 2018). Given that most of the stellar mass in disc galaxies resides in their discs, with $B/T < 0.5$ for most S0 and S galaxies (Graham & Worley 2008), the role of AGN in shaping the *galaxy* stellar-mass function appears limited. Given that mergers, rather than AGN feedback, have likely built the elliptical galaxies which dominate the high-mass end of the galaxy mass function (e.g. Driver et al. 2022), the scope for AGN feedback driving and shaping coevolution in high-mass galaxies appears quenched (e.g., Benson et al. 2003; Ragone-Figueroa et al. 2013; Çatmabacak et al. 2022).

Of course, a galaxy does not need to blow out its gas — via, say, supernovae or an AGN — in order to cause a cessation of star formation. A galaxy could instead prevent the cooling of gas which might form stars (Benson et al. 2003). Creating a hot gas halo in/around massive pressure-supported spheroids may have this effect (e.g., Martín-Navarro et al. 2020, see our Figure 10). While star formation and stellar winds might not generate the escape speeds required to clear gas from a massive galaxy (and its dark matter halo), they contribute a hot gas source, as does gas ‘shock-heating’ during a galaxy collision (e.g., Joshi et al. 2019). X-ray sputtering from hot gas (Galliano et al. 2021) also breaks up dust clouds and

³⁰ The term $\langle I \rangle_{\text{e}}$ is the mean intensity within R_{e} . Given that $M_{*,\text{sph}} \propto R_{\text{e},\text{sph},\text{eq}}^2 \langle I \rangle_{\text{e}}$ (by definition), modulo the (stellar mass)-to-light ratio, and given $M_{*,\text{sph}} \propto R_{\text{e},\text{sph},\text{eq}}^{1.14}$ (Figure 7), we have that $\langle I \rangle_{\text{e}} \propto R_{\text{e},\text{sph},\text{eq}}^{-0.86}$ and thus $M_{*,\text{sph}} \propto \langle I \rangle_{\text{e}}^{-1.33}$.

³¹ We use the term ‘super-linear’ to denote a power-law with a slope steeper than 1 but not as high as 2.

³² We use the term ‘near-quadratic’ to describe a power-law with a slope close to a value of 2.

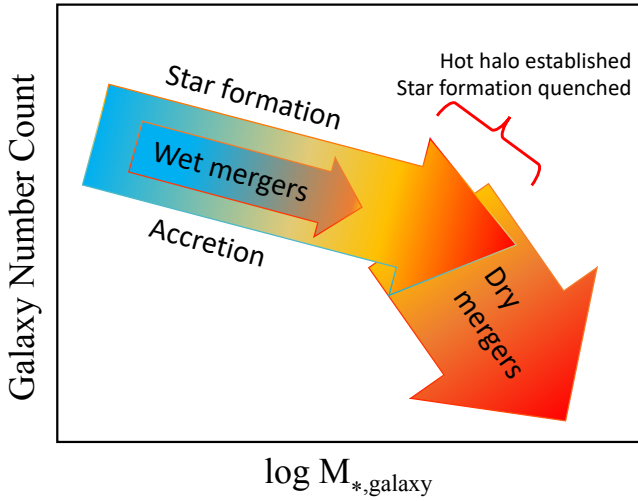


Figure 10. Schematic of the galaxy stellar-mass function. Here we speculate, with reasoning in Section 4.4, as to the nature of the galaxy stellar-mass function. While AGN feedback might regulate bulge growth and help to establish the $M_{\text{bh}}-M_{*,\text{sph}}$ relation in some disc galaxies, it may be the hot gas halo which curtails star formation in discs and keeps it truncated in elliptical galaxies. Mergers, rather than AGN feedback, appear to have established the elliptical galaxy $M_{\text{bh}}-M_{*,\text{sph}}$ relation (Figures 8 and 9).

thereby removes the shielding from ionising radiation that dust may have provided potential stellar nurseries. Furthermore, these winds can keep the AGN ‘pilot light’ on by supplying low-level fuelling (e.g., Ciotti et al. 1991; Soria et al. 2006) for the AGN. We term such an energy source a ‘Benson burner’.³³

Should hot gas halos efficiently suppress star formation, then rather than ejecting gas which might form stars, it is about acquiring and retaining (hot) gas. The system needs to be capable of maintaining, and thus also massive enough to retain, a hot gas halo rather than have it evaporate or collapse into a disk where it may cool and form stars. A *hot ‘n’ dry* (hot gas and dry merger) combination may help explain the upper-end of the galaxy mass function where star formation has dwindled or ceased. Unlike energetic but directional AGN jets (which can both suppress and trigger star formation: Silk 2013; Gaibler 2014; Cresci et al. 2015), a hot gas halo can permeate the entire galaxy, including the disc. The relation between black hole mass and both X-ray gas temperature and luminosity (Bogdán et al. 2018; Gaspari et al. 2019; Lakhchaura et al. 2019) may add credibility to this picture. Low levels of omni-directional particle outflows and electromagnetic radiation from the central ‘Benson burner’ would also help counter cooling (Best et al. 2006; Bower et al. 2006; Croton et al. 2006; Bower et al. 2017) — seen as X-ray radiation coming from the hot gas halo (e.g., Shapiro & Moore 1976; Nulsen et al. 1984). This would help hold star-formation at bay, at least in a closed-box model with no substantial infall of cold gas (e.g., Dekel et al. 2009). When cooler gas is available, sporadic feeding and associated percolation events may produce bubbles and cavities observed at various wavelengths (Sofue & Handa 1984; Tsuboi et al. 1985; Bland-Hawthorn & Cohen 2003; Bîrzan et al. 2004). However, this so-called ‘radio mode’ AGN feedback would

only maintain the $M_{\text{bh}}-M_{*,\text{sph}}$ relation, which we have argued is established by other means (Dubois et al. 2016; Werner et al. 2019).

For the first time, we have used the black hole scaling relations to confirm that AGN primarily have a caretaker role among elliptical galaxies, and we have revealed how mergers rule the roost and dictate the $M_{\text{bh}}/M_{*,\text{sph}}$ ratio and presumably also the $M_{*,\text{sph}}/M_{\text{darkmatter}}$ ratio (Dubois et al. 2016; Marasco et al. 2021). This result is tied to the offset trend seen for elliptical galaxies in the $M_{\text{bh}}-M_{*,\text{sph}}$, $M_{\text{bh}}-M_{*,\text{gal}}$ and $M_{\text{bh}}-R_{\text{e},\text{sph}}$ diagrams. It is not due to spheroids with partially depleted cores, which some E galaxies have but others do not, and which some S0 galaxy bulges possess. Such spheroids, whose central ‘phase space’ is depleted of stars, tend to occupy the $M_{\text{bh}}-M_{*,\text{sph}}$ ‘red sequence’, which is a ‘red herring’ due to the partial picture it provided. In particular, it missed the wet and damp mergers, and thus the steep $M_{\text{bh}}-M_{*,\text{sph}}$ relation for the ensemble of elliptical galaxies. We will pursue this further by addressing merger-built lenticular galaxies with depleted cores, such as NGC 5813, and major wet mergers, for example NGC 5128, in Graham & Sahu (2022).

4.5 Some further thoughts

It is evident that the coevolution of bulges and their central black holes have not produced a simple near-linear $M_{\text{bh}}-M_{*,\text{sph}}$ relation. The steep $M_{\text{bh}}-M_{*,\text{sph}}$ relation for bulges has implications for countless simulations, semi-analytic works, theories, and papers that may have calibrated themselves to a near-linear $M_{\text{bh}}-M_{*,\text{sph}}$ relation. For example, as shown by Bogdán et al. (2018, their Figure 6), while the Horizon-AGN simulation (Dubois et al. 2014) produces an $M_{\text{bh}}-M_{*,\text{sph}}$ ‘red sequence’ with a slope around 1.1 to 1.2, it does not have the scatter to accommodate the steeper relations defined by either the bulges or the elliptical galaxies. That is, it appears to have not captured the key merger-induced jump from bulges to elliptical galaxies. While some studies are ahead of the pack, producing steeper relations (e.g., Fontanot et al. 2006; Dubois et al. 2012; Khandai et al. 2012; Anglés-Alcázar et al. 2017; Weinberger et al. 2018; Delvecchio et al. 2019; Marshall et al. 2020; Irodotou et al. 2022; Tillman et al. 2022), it has been hard for the notion of a steep $M_{\text{bh}}-M_{*,\text{sph}}$ relation to get oxygen given the significant paradigm shift that it implies. It is, therefore, perhaps worth reiterating an element from Graham & Scott (2013, their section 4.3), which introduced a related revision to the ‘quasar mode’ (aka cold-gas mode) of black hole growth used in some semi-analytic models (Granato et al. 2004; Springel et al. 2005).

The steep $M_{\text{bh}}-M_{\text{dyn},\text{sph}}$ relation detected by Graham (2012), which supplanted the single linear relation from Häring & Rix (2004), challenged the past assumption of accretion-induced black hole growth that is linearly proportional to the inflowing mass of cold gas. Croton et al. (2006, their Equation 8) and others have popularised this black hole feeding scenario to model how AGN outflows account for what was thought to be a linear $M_{\text{bh}}-M_{*,\text{sph}}$ relation. Graham & Scott (2013) presented a revised prescription for the increase in black hole mass, δM_{bh} , associated with wet mergers, such that

$$\delta M_{\text{bh}} \propto \left(\frac{M_{\text{min}}}{M_{\text{maj}}} \right) \left[\frac{M_{\text{cold}}^X}{1 + (280 \text{ km s}^{-1})/V_{\text{virial}}} \right]. \quad (6)$$

The exponent X represents the logarithmic slope of the $M_{\text{bh}}-M_{*,\text{sph}}$ relation for bulges, and they specified $X = 2$. M_{min} and M_{maj} are the total baryonic masses from the minor and major galaxies involved in the accretion/merger event, and M_{cold} is their combined cold gas mass. The velocity V_{virial} is the merged system’s circular or

³³ This is a play on words combining Bunsen burner - used for heating and sterilisation - and a reference to the idea sparked by (Benson et al. 2003).

‘virial’ velocity, normalised at 280 km s^{-1} (Kauffmann & Haehnelt 2000). This modified equation may prove helpful for exploring and understanding galaxy/(black hole) evolution through semi-analytic approaches, although it does not encompass the cessation of star-formation due to hot X-ray halos in massive systems, or the pivotal role of dry mergers in shaping the distribution seen in the $M_{\text{bh}}-M_{*,\text{sph}}$ diagram.

There are also significant ramifications for predictions of gravitational waves from space-based interferometers (e.g., Merritt & Milosavljević 2005; Sesana 2013; Khan et al. 2020; Santoliquido et al. 2022) and pulsar timing arrays monitored with ground-based radio telescopes (e.g., Hobbs et al. 2010; Shannon et al. 2013; Chen et al. 2019). For example, the steep $M_{\text{bh}}-M_{*,\text{sph}}$ relation for bulges should be considered, if not favoured over the near-linear ‘red-sequence’ when assigning BH masses to galaxies in works attempting to estimate the background signal from binary black hole mergers. One caveat here is that the mergers involving a BCG may involve systems on both the bulge and the elliptical sequence. As noted in Graham & Soria (2019), predictions for black hole masses will be too high if using the original near-linear $M_{\text{bh}}-M_{*,\text{sph}}$ relation at low spheroid masses. This over-prediction can result in over-looking potential populations of intermediate-mass black holes ($10^2 < M_{\text{bh}}/M_{\odot} < 10^5$). Furthermore, application of the steeper relation has already been shown to result in an order of magnitude reduction to the expected detection rate of extreme mass ratio inspiral (EMRI) events from compact stellar-mass objects around massive black holes (e.g., Mapelli et al. 2012). That work can be further refined based on the updated relations herein, providing better expectations for what the European Laser Interferometer Space Antenna (LISA) (Danzmann & LISA Study Team 1997) and TianQin (Luo et al. 2016) can hope to achieve based on their current design plans.

As noted above, the pursuit of long-wavelength gravitational waves, from the coalescence of binary supermassive black holes (e.g., Komossa et al. 2003; Rodriguez et al. 2006; Liu et al. 2019; O’Neill et al. 2022), is an endeavour underway via monitoring pulsar arrival times using radio telescopes. These studies will benefit from an improved knowledge of the varying $M_{\text{bh}}/M_{*,\text{sph}}$, and $M_{\text{bh}}/M_{*,\text{gal}}$, ratios in pre-merged galaxies. This can enable revised predictions for, and possibly aid in the tentative confirmation of, a long-wavelength gravitational wave background (Arzoumanian et al. 2020; Chen et al. 2021).

Related to the EMRI events are the nuclear stars clusters that coexist with (e.g., González Delgado et al. 2008; Seth et al. 2008; Graham & Spitler 2009) and feed (e.g., Komossa 2002; Li et al. 2002) the central black hole in galaxies. The revised/steeper $M_{\text{bh}}-M_{*,\text{sph}}$ relations, coupled with the $M_{\text{nsc}}-M_{*,\text{sph}}$ relations (Balcells et al. 2003; Graham & Guzmán 2003), led to the discovery of the $M_{\text{bh}}-M_{\text{nsc}}$ relation (Graham 2016a, 2020). This should be useful for modelling not only gravitational radiation events but also the expected frequency of tidal disruption events (TDEs: Komossa & Dahlem 2001; Wang & Merritt 2004; Komossa 2015; Stone & Metzger 2016; Coughlin et al. 2017; Toscani et al. 2020), which have been observed in data dating back to 1990. There are currently around 100 such known events.³⁴

If a non-rotating Schwarzschild-Droste (Schwarzschild 1916; Droste 1917) black hole is more massive than $\sim 10^8 M_{\odot}$, and thus the gravitational gradient at, and beyond, the ‘event horizon’ is not strong enough to pull a star apart, there will be no TDE (Magorrian

& Tremaine 1999). The star will cross the event horizon and disappear without displaying its hot interior. As we have seen, most of the systems with $M_{\text{bh}} \lesssim 10^8 M_{\odot}$ follow the near-quadratic $M_{\text{bh}}-M_{*,\text{sph}}$ relation for bulges, suggesting the need to use this steeper relation rather than the near-linear ‘red-sequence’, which pertains to (some) systems with $M_{\text{bh}} \gtrsim 10^8 M_{\odot}$. One should, however, be mindful that the spin-reduced size of the event horizon in a rotating Kerr (1963) black hole can result in a star’s tidal disruption radius being greater than the event horizon for black hole masses up to $\sim 7 \times 10^8 M_{\odot}$ for maximally spinning black holes (Beloborodov et al. 1992; Kesden 2012).

The morphology-dependent black hole scaling relations also demand a re-examination of the virial f -factors used to convert AGN virial masses into black hole masses (e.g., Bentz et al. 2009; Bentz & Manne-Nicholas 2018). Failing to account for the different morphologies and formation history of the spheroids hosting the AGN or inactive black holes will produce erroneous results.

As noted in Graham (2012), there is a wealth of additional and immediate implications and insight from the steeper-than-linear $M_{\text{bh}}-M_{*,\text{sph}}$ relations. These include black hole mass predictions in other galaxies, constructing the black hole mass function, and deriving the black hole mass density based on reliable bulge and elliptical galaxy mass functions. In passing, it is noted that some care with the Hubble-Lemaître constant, or little h , is required for such calculations, as noted in Graham & Driver (2007a) and Croton (2013).

ACKNOWLEDGEMENTS

This research was supported under the Australian Research Council’s funding scheme DP17012923. Part of this research was conducted within the Australian Research Council’s Centre of Excellence for Gravitational Wave Discovery (OzGrav), through project number CE170100004. This research has made use of the NASA/IPAC Extragalactic Database (NED) and the NASA/IPAC Infrared Science Archive. We used the RSTAN package available at <https://mc-stan.org/>. We also used python packages numpy (Harris et al. 2020), matplotlib (Hunter 2007) and SciPy (Virtanen et al. 2020).

5 DATA AVAILABILITY

The data underlying this article are available in the NASA/IPAC Infrared Science Archive.

REFERENCES

- Akritas M. G., Bershadsky M. A., 1996, *ApJ*, **470**, 706
- Anglés-Alcázar D., Faucher-Giguère C.-A., Quataert E., Hopkins P. F., Feldmann R., Torrey P., Wetzel A., Kereš D., 2017, *MNRAS*, **472**, L109
- Arzoumanian Z., et al., 2020, *ApJ*, **905**, L34
- Athanassoula E., 2005, *MNRAS*, **358**, 1477
- Balcells M., Peletier R. F., 1994, *AJ*, **107**, 135
- Balcells M., Graham A. W., Domínguez-Palmero L., Peletier R. F., 2003, *ApJ*, **582**, L79
- Baldassare V. F., Reines A. E., Gallo E., Greene J. E., 2015, *ApJ*, **809**, L14
- Baldassare V. F., Reines A. E., Gallo E., Greene J. E., 2017, *ApJ*, **850**, 196
- Barth A. J., Ho L. C., Rutledge R. E., Sargent W. L. W., 2004, *ApJ*, **607**, 90
- Bell E. F., de Jong R. S., 2001, *ApJ*, **550**, 212
- Bell E. F., McIntosh D. H., Katz N., Weinberg M. D., 2003, *ApJS*, **149**, 289

³⁴ <https://tde.space/>

- Beloborodov A. M., Illarionov A. F., Ivanov P. B., Polnarev A. G., 1992, *MNRAS*, **259**, 209
- Benson A. J., Bower R. G., Frenk C. S., Lacey C. G., Baugh C. M., Cole S., 2003, *ApJ*, **599**, 38
- Bentz M. C., Manne-Nicholas E., 2018, *ApJ*, **864**, 146
- Bentz M. C., Peterson B. M., Pogge R. W., Vestergaard M., 2009, *ApJ*, **694**, L166
- Bernardi M., Shankar F., Hyde J. B., Mei S., Marulli F., Sheth R. K., 2010, *MNRAS*, **404**, 2087
- Best P. N., Kaiser C. R., Heckman T. M., Kauffmann G., 2006, *MNRAS*, **368**, L67
- Bîrzan L., Rafferty D. A., McNamara B. R., Wise M. W., Nulsen P. E. J., 2004, *ApJ*, **607**, 800
- Blais-Ouellette S., Amram P., Carignan C., Swaters R., 2004, *A&A*, **420**, 147
- Blakeslee J. P., Lucey J. R., Tonry J. L., Hudson M. J., Narayanan V. K., Barris B. J., 2002, *MNRAS*, **330**, 443
- Blakeslee J. P., et al., 2009, *ApJ*, **694**, 556
- Blakeslee J. P., et al., 2010, *ApJ*, **724**, 657
- Bland-Hawthorn J., Cohen M., 2003, *ApJ*, **582**, 246
- Blom C., Forbes D. A., Foster C., Romanowsky A. J., Brodie J. P., 2014, *MNRAS*, **439**, 2420
- Bogdán Á., Lovisari L., Volonteri M., Dubois Y., 2018, *ApJ*, **852**, 131
- Boizelle B. D., et al., 2021, *ApJ*, **908**, 19
- Boselli A., Fossati M., Gavazzi G., Ciesla L., Buat V., Boissier S., Hughes T. M., 2015, *A&A*, **579**, A102
- Bower R. G., Benson A. J., Malbon R., Helly J. C., Frenk C. S., Baugh C. M., Cole S., Lacey C. G., 2006, *MNRAS*, **370**, 645
- Bower R. G., Schaye J., Frenk C. S., Theuns T., Schaller M., Crain R. A., McAlpine S., 2017, *MNRAS*, **465**, 32
- Bresolin F., 2013, *ApJ*, **772**, L23
- Burkert A., Tremaine S., 2010, *ApJ*, **720**, 516
- Capetti A., Marconi A., Macchetto D., Axon D., 2005, *A&A*, **431**, 465
- Carpenter B., et al., 2017, *Journal of Statistical Software*, **76**, 1
- Cecil G., Bland-Hawthorn J., Veilleux S., Filippenko A. V., 2001, *ApJ*, **555**, 338
- Chabrier G., 2003, *PASP*, **115**, 763
- Chen S., Sesana A., Conselice C. J., 2019, *MNRAS*, **488**, 401
- Chen S., et al., 2021, *MNRAS*, **508**, 4970
- Ciambur B. C., 2015, *ApJ*, **810**, 120
- Ciambur B. C., Graham A. W., 2016, *MNRAS*, **459**, 1276
- Ciotti L., D’Ercole A., Pellegrini S., Renzini A., 1991, *ApJ*, **376**, 380
- Cisternas M., et al., 2011, *ApJ*, **726**, 57
- Combes F., Sanders R. H., 1981, *A&A*, **96**, 164
- Cortés J. R., Kenney J. D. P., Hardy E., 2008, *ApJ*, **683**, 78
- Coughlin E. R., Armitage P. J., Nixon C., Begelman M. C., 2017, *MNRAS*, **465**, 3840
- Cresci G., et al., 2015, *ApJ*, **799**, 82
- Croton D. J., 2013, *Publ. Astron. Soc. Australia*, **30**, e052
- Croton D. J., et al., 2006, *MNRAS*, **365**, 11
- Daddi E., et al., 2005, *ApJ*, **626**, 680
- Damjanov I., et al., 2011, *ApJ*, **739**, L44
- Danzmann K., LISA Study Team 1997, *Classical and Quantum Gravity*, **14**, 1399
- Davis B. L., Graham A. W., Cameron E., 2018, *ApJ*, **869**, 113
- Davis B. L., Graham A. W., Cameron E., 2019, *ApJ*, **873**, 85
- Davis T. A., et al., 2020, *MNRAS*, **496**, 4061
- Dekel A., et al., 2009, *Nature*, **457**, 451
- Delvecchio I., et al., 2019, *ApJ*, **885**, L36
- Devereux N., 2018, *MNRAS*, **473**, 2930
- Di Matteo T., Colberg J., Springel V., Hernquist L., Sijacki D., 2008, *ApJ*, **676**, 33
- Dressler A., 1989, in Osterbrock D. E., Miller J. S., eds, *IAU Symposium Vol. 134, Active Galactic Nuclei*. Kluwer Academic Publishers, Dordrecht, p. 217
- Dressler A., Richstone D. O., 1988, *ApJ*, **324**, 701
- Driver S. P., Popescu C. C., Tuffs R. J., Liske J., Graham A. W., Allen P. D., de Propriis R., 2007, *MNRAS*, **379**, 1022
- Driver S. P., et al., 2022, *MNRAS*, **513**, 439
- Droste J., 1917, *Koninklijke Nederlandse Akademie van Wetenschappen Proceedings Series B Physical Sciences*, **19**, 197
- Drouart G., et al., 2014, *A&A*, **566**, A53
- Dubois Y., Devriendt J., Slyz A., Teyssier R., 2012, *MNRAS*, **420**, 2662
- Dubois Y., et al., 2014, *MNRAS*, **444**, 1453
- Dubois Y., Peirani S., Pichon C., Devriendt J., Gavazzi R., Welker C., Volonteri M., 2016, *MNRAS*, **463**, 3948
- Dullo B. T., 2019, *ApJ*, **886**, 80
- Dullo B. T., Bouquin A. Y. K., Gil de Paz A., Knapen J. H., Gorgas J., 2020, *ApJ*, **898**, 83
- Erwin P., Beltrán J. C. V., Graham A. W., Beckman J. E., 2003, *ApJ*, **597**, 929
- Event Horizon Telescope Collaboration et al., 2019a, *ApJ*, **875**, L1
- Event Horizon Telescope Collaboration et al., 2019b, *ApJ*, **875**, L6
- Fazio G. G., et al., 2004, *ApJS*, **154**, 10
- Ferrarese L., Ford H., 2005, *Space Sci. Rev.*, **116**, 523
- Ferré-Mateu A., Trujillo I., Martín-Navarro I., Vazdekis A., Mezcua M., Balcells M., Domínguez L., 2017, *MNRAS*, **467**, 1929
- Florez J., et al., 2020, *MNRAS*, **497**, 3273
- Flynn C., Holmberg J., Portinari L., Fuchs B., Jahreiß H., 2006, *MNRAS*, **372**, 1149
- Fontanot F., Monaco P., Cristiani S., Tozzi P., 2006, *MNRAS*, **373**, 1173
- Gabor J. M., Bournaud F., 2014, *MNRAS*, **441**, 1615
- Gabor J. M., et al., 2009, *ApJ*, **691**, 705
- Gaibler V., 2014, *Astronomische Nachrichten*, **335**, 531
- Galliano F., et al., 2021, *A&A*, **649**, A18
- García-Benito R., González Delgado R. M., Pérez E., Cid Fernandes R., Sánchez S. F., de Amorim A. L., 2019, *A&A*, **621**, A120
- Gaspari M., Ruszkowski M., Oh S. P., 2013, *MNRAS*, **432**, 3401
- Gaspari M., et al., 2019, *ApJ*, **884**, 169
- González Delgado R. M., Pérez E., Cid Fernandes R., Schmitt H., 2008, *AJ*, **135**, 747
- Graham A. W., 2007, *MNRAS*, **379**, 711
- Graham A. W., 2012, *ApJ*, **746**, 113
- Graham A. W., 2016a, in Meiron Y., Li S., Liu F. K., Spurzem R., eds, *IAU Symposium Vol. 312, Star Clusters and Black Holes in Galaxies across Cosmic Time*. pp 269–273 ([arXiv:1412.5715](https://arxiv.org/abs/1412.5715)), doi:10.1017/S1743921315008017
- Graham A. W., 2016b, in Laurikainen E., Peletier R., Gadotti D., eds, *Astrophysics and Space Science Library Vol. 418, Galactic Bulges*. p. 263 ([arXiv:1501.02937](https://arxiv.org/abs/1501.02937)), doi:10.1007/978-3-319-19378-6_11
- Graham A. W., 2019, *MNRAS*, **487**, 4995
- Graham A. W., 2020, *MNRAS*, **492**, 3263
- Graham A. W., Driver S. P., 2005, *Publ. Astron. Soc. Australia*, **22**, 118
- Graham A. W., Driver S. P., 2007a, *MNRAS*, **380**, L15
- Graham A. W., Driver S. P., 2007b, *ApJ*, **655**, 77
- Graham A. W., Guzmán R., 2003, *AJ*, **125**, 2936
- Graham A. W., Sahu N., 2022, *MNRAS*, submitted
- Graham A. W., Scott N., 2013, *ApJ*, **764**, 151
- Graham A. W., Scott N., 2015, *ApJ*, **798**, 54
- Graham A. W., Soria R., 2019, *MNRAS*, **484**, 794
- Graham A. W., Spitler L. R., 2009, *MNRAS*, **397**, 2148
- Graham A. W., Worley C. C., 2008, *MNRAS*, **388**, 1708
- Graham A. W., Erwin P., Trujillo I., Asensio Ramos A., 2003, *AJ*, **125**, 2951
- Graham A. W., Merritt D., Moore B., Diemand J., Terzić B., 2006, *AJ*, **132**, 2711
- Graham A. W., Onken C. A., Athanassoula E., Combes F., 2011, *MNRAS*, **412**, 2211
- Graham A. W., Dullo B. T., Savorgnan G. A. D., 2015, *ApJ*, **804**, 32
- Graham A. W., Ciambur B. C., Soria R., 2016a, *ApJ*, **818**, 172
- Graham A. W., Ciambur B. C., Savorgnan G. A. D., 2016b, *ApJ*, **831**, 132
- Graham A. W., Janz J., Penny S. J., Chilingarian I. V., Ciambur B. C., Forbes D. A., Davies R. L., 2017, *ApJ*, **840**, 68
- Graham A. W., Soria R., Ciambur B. C., Davis B. L., Swartz D. A., 2021, *ApJ*, **923**, 146
- Granato G. L., De Zotti G., Silva L., Bressan A., Danese L., 2004, *ApJ*, **600**, 580

- Grogan N. A., et al., 2005, *ApJ*, **627**, L97
- Häring N., Rix H.-W., 2004, *ApJ*, **604**, L89
- Harris C. R., et al., 2020, *Nature*, **585**, 357
- Hobbs G., et al., 2010, *Classical and Quantum Gravity*, **27**, 084013
- Hogg D. W., Bovy J., Lang D., 2010, arXiv e-prints, p. arXiv:1008.4686
- Hon D. S. H., Graham A. W., Davis B. L., Marconi A., 2022a, *MNRAS*, **514**, 3410
- Hon D. S. H., Graham A. W., Sahu N., 2022b, *MNRAS*, submitted
- Hönig S. F., Watson D., Kishimoto M., Hjorth J., 2014, *Nature*, **515**, 528
- Humphreys E. M. L., Reid M. J., Moran J. M., Greenhill L. J., Argon A. L., 2013, *ApJ*, **775**, 13
- Hunter J. D., 2007, *Computing in Science & Engineering*, **9**, 90
- Into T., Portinari L., 2013, *MNRAS*, **430**, 2715
- Irodotou D., et al., 2022, *MNRAS*, **513**, 3768
- Jensen J. B., et al., 2021, *ApJS*, **255**, 21
- Joshi B. A., et al., 2019, *ApJ*, **878**, 161
- Karachentsev I. D., Nasonova O. G., 2013, *MNRAS*, **429**, 2677
- Karachentsev I. D., et al., 2002, *A&A*, **389**, 812
- Karachentsev I. D., et al., 2007, *AJ*, **133**, 504
- Karachentsev I. D., Nasonova O. G., Karachentseva V. E., 2015, *Astrophysical Bulletin*, **70**, 1
- Kauffmann G., Haehnelt M., 2000, *MNRAS*, **311**, 576
- Kelly B. C., 2007, *ApJ*, **665**, 1489
- Kerr R. P., 1963, *Phys. Rev. Lett.*, **11**, 237
- Kesden M., 2012, *Phys. Rev. D*, **85**, 024037
- Khan F. M., Mirza M. A., Holley-Bockelmann K., 2020, *MNRAS*, **492**, 256
- Khandai N., Feng Y., DeGraf C., Di Matteo T., Croft R. A. C., 2012, *MNRAS*, **423**, 2397
- King I. R., Minkowski R., 1966, *ApJ*, **143**, 1002
- King I. R., Minkowski R., 1972, in Evans D. S., Wills D., Wills B. J., eds, *IAU Symposium Vol. 44, External Galaxies and Quasi-Stellar Objects*. p. 87
- Kisaka S., Kojima Y., Otani Y., 2008, *MNRAS*, **390**, 814
- Kocevski D. D., et al., 2012, *ApJ*, **744**, 148
- Komossa S., 2002, *Reviews in Modern Astronomy*, **15**, 27
- Komossa S., 2015, *Journal of High Energy Astrophysics*, **7**, 148
- Komossa S., Dahlem M., 2001, arXiv e-prints, pp astro-ph/0106422
- Komossa S., Burwitz V., Hasinger G., Predehl P., Kaastra J. S., Ikebe Y., 2003, *ApJ*, **582**, L15
- Kormendy J., Ho L. C., 2013, *ARA&A*, **51**, 511
- Krajinović D., Emsellem E., den Brok M., Marino R. A., Schmidt K. B., Steinmetz M., Weilbacher P. M., 2018, *MNRAS*, **477**, 5327
- Kroupa P., 1998, in Rebolo R., Martin E. L., Zapatero Osorio M. R., eds, *Astronomical Society of the Pacific Conference Series Vol. 134, Brown Dwarfs and Extrasolar Planets*. p. 483
- Kroupa P., 2001, *MNRAS*, **322**, 231
- Kroupa P., 2002, *Science*, **295**, 82
- Kroupa P., Weidner C., Pflamm-Altenburg J., Thies I., Dabringhausen J., Marks M., Maschberger T., 2013, in Oswalt T. D., Gilmore G., eds, *Planets, Stars and Stellar Systems Vol. 5, Planets, Stars and Stellar Systems. Volume 5: Galactic Structure and Stellar Populations*. p. 115, doi:10.1007/978-94-007-5612-0_4
- Kudritzki R.-P., Urbaneja M. A., Gazak Z., Bresolin F., Przybilla N., Gieren W., Pietrzyński G., 2012, *ApJ*, **747**, 15
- Kundu A., Whitmore B. C., 1998, *AJ*, **116**, 2841
- Kuntschner H., Ziegler B. L., Sharples R. M., Worthey G., Fricke K. J., 2002, *A&A*, **395**, 761
- LaMassa S. M., Heckman T. M., Ptak A., Urry C. M., 2013, *ApJ*, **765**, L33
- Lakhchaura K., Truong N., Werner N., 2019, *MNRAS*, **488**, L134
- Laor A., 1998, *ApJ*, **505**, L83
- Laor A., 2001, *ApJ*, **553**, 677
- Lauer T. R., Faber S. M., Ajhar E. A., Grillmair C. J., Scowen P. A., 1998, *AJ*, **116**, 2263
- Laurikainen E., Salo H., Buta R., 2005, *MNRAS*, **362**, 1319
- Laurikainen E., Salo H., Knapen J. H., 2011, *MNRAS*, **418**, 1452
- Li L.-X., Narayan R., Menou K., 2002, *ApJ*, **576**, 753
- Liller M. H., 1966, *ApJ*, **146**, 28
- Liu T., et al., 2019, *ApJ*, **884**, 36
- Longair M. S. M. S., 2006, *The cosmic century : a history of astrophysics and cosmology*. Cambridge University Press, Cambridge, UK
- Luo J., et al., 2016, *Classical and Quantum Gravity*, **33**, 035010
- MacArthur L. A., González J. J., Courteau S., 2009, *MNRAS*, **395**, 28
- Madau P., Dickinson M., 2014, *ARA&A*, **52**, 415
- Magorrian J., Tremaine S., 1999, *MNRAS*, **309**, 447
- Magorrian J., et al., 1998, *AJ*, **115**, 2285
- Mapelli M., Ripamonti E., Vecchio A., Graham A. W., Gualandris A., 2012, *A&A*, **542**, A102
- Marasco A., Cresci G., Posti L., Fraternali F., Mannucci F., Marconi A., Belfiore F., Fall S. M., 2021, *MNRAS*, **507**, 4274
- Marshall M. A., Mutch S. J., Qin Y., Poole G. B., Wyithe J. S. B., 2020, *MNRAS*, **494**, 2747
- Martin-Navarro I., Burchett J. N., Mezcuca M., 2020, *MNRAS*, **491**, 1311
- McGaugh S. S., Schombert J. M., 2014, *AJ*, **148**, 77
- McQuinn K. B. W., Skillman E. D., Dolphin A. E., Berg D., Kennicutt R., 2016, *AJ*, **152**, 144
- McQuinn K. B. W., Skillman E. D., Dolphin A. E., Berg D., Kennicutt R., 2017, *AJ*, **154**, 51
- Mei S., Silva D., Quinn P. J., 2000, *A&A*, **361**, 68
- Meidt S. E., et al., 2014, *ApJ*, **788**, 144
- Merritt D., Milosavljević M., 2005, *Living Reviews in Relativity*, **8**, 8
- Mieske S., Küpper A. H. W., Brockamp M., 2014, *A&A*, **565**, L6
- Monachesi A., Bell E. F., Radburn-Smith D. J., Bailin J., de Jong R. S., Holwerda B., Streich D., Silverstein G., 2016, *MNRAS*, **457**, 1419
- Naab T., Khochfar S., Burkert A., 2006, *ApJ*, **636**, L81
- Nasonova O. G., de Freitas Pacheco J. A., Karachentsev I. D., 2011, *A&A*, **532**, A104
- Nguyen D. D., et al., 2017, *ApJ*, **836**, 237
- Nipoti C., Treu T., Bolton A. S., 2009a, *ApJ*, **703**, 1531
- Nipoti C., Treu T., Auger M. W., Bolton A. S., 2009b, *ApJ*, **706**, L86
- Novak G. S., Faber S. M., Dekel A., 2006, *ApJ*, **637**, 96
- Nulsen P. E. J., Stewart G. C., Fabian A. C., 1984, *MNRAS*, **208**, 185
- O'Neill S., et al., 2022, *ApJ*, **926**, L35
- Peletier R. F., Balcells M., 1996, *AJ*, **111**, 2238
- Peletier R. F., Balcells M., Davies R. L., Andredakis Y., Vazdekis A., Burkert A., Prada F., 1999, *MNRAS*, **310**, 703
- Peng C. Y., 2007, *ApJ*, **671**, 1098
- Pietrzyński G., et al., 2019, *Nature*, **567**, 200
- Poggianti B. M., Moretti A., Calvi R., D'Onofrio M., Valentinuzzi T., Fritz J., Renzini A., 2013, *ApJ*, **777**, 125
- Popescu C. C., Misiriotis A., Kyllafis N. D., Tuffs R. J., Fischera J., 2000, *A&A*, **362**, 138
- Portinari L., Sommer-Larsen J., Tantalo R., 2004, *MNRAS*, **347**, 691
- Pota V., Graham A. W., Forbes D. A., Romanowsky A. J., Brodie J. P., Strader J., 2013, *MNRAS*, **433**, 235
- Querejeta M., et al., 2015, *ApJS*, **219**, 5
- Radburn-Smith D. J., et al., 2011, *ApJS*, **195**, 18
- Ragone-Figueroa C., Granato G. L., Murante G., Borgani S., Cui W., 2013, *MNRAS*, **436**, 1750
- Reid M. J., Braatz J. A., Condon J. J., Lo K. Y., Kuo C. Y., Impellizzeri C. M. V., Henkel C., 2013, *ApJ*, **767**, 154
- Riess A. G., Fliri J., Valls-Gabaud D., 2012, *ApJ*, **745**, 156
- Roche E. A., 1850, *Montpellier Academy of Sciences and Letters. Mémoires de la section des sciences*, **1**, 333
- Rodriguez C., Taylor G. B., Zavala R. T., Peck A. B., Pollack L. K., Romani R. W., 2006, *ApJ*, **646**, 49
- Rodríguez Ó., Clocchiatti A., Hamuy M., 2014, *AJ*, **148**, 107
- Roediger J. C., Courteau S., 2015, *MNRAS*, **452**, 3209
- Sabbi E., et al., 2018, *ApJS*, **235**, 23
- Sadoun R., Colin J., 2012, *MNRAS*, **426**, L51
- Saglia R. P., et al., 2016, *ApJ*, **818**, 47
- Sahu N., Graham A. W., Davis B. L., 2019a, *ApJ*, **876**, 155
- Sahu N., Graham A. W., Davis B. L., 2019b, *ApJ*, **887**, 10
- Sahu N., Graham A. W., Davis B. L., 2020, *ApJ*, **903**, 97
- Sahu N., Graham A. W., Davis B. L., 2022a, *ApJ*, **927**, 67
- Sahu N., Graham A. W., Hon D. S.-H., 2022b, *MNRAS*, submitted
- Salucci P., Ratnam C., Monaco P., Danese L., 2000, *MNRAS*, **317**, 488

- Santoliquido F., Mapelli M., Artale M. C., Boco L., 2022, arXiv e-prints, p. [arXiv:2205.05099](#)
- Saracco P., Longhetti M., Gargiulo A., 2010, *MNRAS*, **408**, L21
- Savorgnan G. A. D., Graham A. W., 2016, *ApJS*, **222**, 10
- Savorgnan G. A. D., Graham A. W., Marconi A., Sani E., 2016, *ApJ*, **817**, 21
- Schaye J., et al., 2010, *MNRAS*, **402**, 1536
- Schlaflly E. F., Finkbeiner D. P., 2011, *ApJ*, **737**, 103
- Schombert J., McGaugh S., Lelli F., 2019, *MNRAS*, **483**, 1496
- Schombert J., McGaugh S., Lelli F., 2022, arXiv e-prints, p. [arXiv:2202.02290](#)
- Schwarzschild K., 1916, Abh. Konigl. Preuss. Akad. Wissenschaften Jahre 1906/92, Berlin, 1907, **1916**, 189
- Scott N., Graham A. W., Schombert J., 2013, *ApJ*, **768**, 76
- Sérsic J. L., 1963, Boletín de la Asociacion Argentina de Astronomia La Plata Argentina, **6**, 41
- Sesana A., 2013, *Classical and Quantum Gravity*, **30**, 244009
- Seth A., Agüeros M., Lee D., Basu-Zych A., 2008, *ApJ*, **678**, 116
- Seymour N., et al., 2012, *ApJ*, **755**, 146
- Shankar F., et al., 2016, *MNRAS*, **460**, 3119
- Shannon R. M., et al., 2013, *Science*, **342**, 334
- Shapiro P. R., Moore R. T., 1976, *ApJ*, **207**, 460
- Sijacki D., Springel V., Di Matteo T., Hernquist L., 2007, *MNRAS*, **380**, 877
- Silk J., 2013, *ApJ*, **772**, 112
- Silk J., Rees M. J., 1998, *A&A*, **331**, L1
- Smith M. D., et al., 2021a, *MNRAS*, **500**, 1933
- Smith M. D., et al., 2021b, *MNRAS*, **503**, 5984
- Sofue Y., Handa T., 1984, *Nature*, **310**, 568
- Sorce J. G., Tully R. B., Courtois H. M., Jarrett T. H., Neill J. D., Shaya E. J., 2014, *MNRAS*, **444**, 527
- Soria R., Graham A. W., Fabbiano G., Baldi A., Elvis M., Jerjen H., Pellegrini S., Siemiginowska A., 2006, *ApJ*, **640**, 143
- Spitler L. R., Forbes D. A., 2009, *MNRAS*, **392**, L1
- Spolaor M., Proctor R. N., Forbes D. A., Couch W. J., 2009, *ApJ*, **691**, L138
- Springel V., Di Matteo T., Hernquist L., 2005, *MNRAS*, **361**, 776
- Stone N. C., Metzger B. D., 2016, *MNRAS*, **455**, 859
- Su M., Slatyer T. R., Finkbeiner D. P., 2010, *ApJ*, **724**, 1044
- Taylor E. N., et al., 2011, *MNRAS*, **418**, 1587
- Team S. D., 2016, RStan: the interface to Stan, Version 2.14.1, <http://mc>
- Theureau G., Hanski M. O., Coudreau N., Hallet N., Martin J. M., 2007, *A&A*, **465**, 71
- Thornton C. E., Barth A. J., Ho L. C., Rutledge R. E., Greene J. E., 2008, *ApJ*, **686**, 892
- Tillman M. T., Wellons S., Faucher-Giguère C.-A., Kelley L. Z., Anglés-Alcázar D., 2022, *MNRAS*, **511**, 5756
- Tonry J. L., Dressler A., Blakeslee J. P., Ajhar E. A., Fletcher A. B., Luppino G. A., Metzger M. R., Moore C. B., 2001, *ApJ*, **546**, 681
- Toomre A., Toomre J., 1972, *ApJ*, **178**, 623
- Toscani M., Rossi E. M., Lodato G., 2020, *MNRAS*, **498**, 507
- Tremaine S., et al., 2002, *ApJ*, **574**, 740
- Trujillo I., Ferré-Mateu A., Balcells M., Vazdekis A., Sánchez-Blázquez P., 2014, *ApJ*, **780**, L20
- Tsuboi M., Inoue M., Handa T., Tabara H., Kato T., 1985, *PASJ*, **37**, 359
- Tully R. B., Shaya E. J., Karachentsev I. D., Courtois H. M., Kocevski D. D., Rizzi L., Peel A., 2008, *ApJ*, **676**, 184
- Tully R. B., Rizzi L., Shaya E. J., Courtois H. M., Makarov D. I., Jacobs B. A., 2009, *AJ*, **138**, 323
- Valentinuzzi T., et al., 2010, *ApJ*, **712**, 226
- Virtanen P., et al., 2020, *Nature Methods*, **17**, 261
- Wandel A., 1999, *ApJ*, **519**, L39
- Wang J., Merritt D., 2004, *ApJ*, **600**, 149
- Warner C., Hamann F., Dietrich M., 2003, *ApJ*, **596**, 72
- Weinberger R., et al., 2018, *MNRAS*, **479**, 4056
- Werner N., McNamara B. R., Churazov E., Scannapieco E., 2019, *Space Sci. Rev.*, **215**, 5
- Williams B. F., Dalcanton J. J., Gilbert K. M., Stilp A., Dolphin A., Seth A. C., Weisz D., Skillman E., 2010, *ApJ*, **716**, 71
- Willmer C. N. A., 2018, *ApJS*, **236**, 47
- Yamauchi A., Nakai N., Ishihara Y., Diamond P., Sato N., 2012, *PASJ*, **64**, 103
- Yee H. K. C., 1992, in Filippenko A. V., ed., *Astronomical Society of the Pacific Conference Series Vol. 31, Relationships Between Active Galactic Nuclei and Starburst Galaxies*. p. 417
- Zhang H.-X., Puzia T. H., Weisz D. R., 2017, *ApJS*, **233**, 13
- Zhao W., et al., 2018, *ApJ*, **854**, 124
- Zibetti S., Charlot S., Rix H.-W., 2009, *MNRAS*, **400**, 1181
- Zwicky F., 1966, *ApJ*, **143**, 192
- Zwicky F., Kowal C. T., 1968, “Catalogue of Galaxies and of Clusters of Galaxies”, Volume VI. California Institute of Technology, Pasadena
- Zwicky F., Zwicky M. A., 1971, Catalogue of selected compact galaxies and of post-eruptive galaxies. Guemligen, Switzerland
- Çatmabacak O., Feldmann R., Anglés-Alcázar D., Faucher-Giguère C.-A., Hopkins P. F., Kereš D., 2022, *MNRAS*, **511**, 506
- de Vaucouleurs G., de Vaucouleurs A., Corwin Herold G. J., Buta R. J., Paturel G., Fouque P., 1991, Third Reference Catalogue of Bright Galaxies. Springer, New York
- de la Rosa I. G., La Barbera F., Ferreras I., Sánchez Almeida J., Dalla Vecchia C., Martínez-Valpuesta I., Stringer M., 2016, *MNRAS*, **457**, 1916
- van den Bosch R. C. E., 2016, *ApJ*, **831**, 134

APPENDIX A: NIR-OPTICAL COLOURS AND AN ALTERNATIVE (STELLAR MASS)-TO-LIGHT RATIO, Υ

As reported by [Into & Portinari \(2013\)](#), and previously noticed by [Bell & de Jong \(2001\)](#), optical-NIR colours are better indicators of metallicity than stellar mass-to-light ratios. They lack the sensitivity to age which the optical colours can have. Ironically, this may be advantageous for our situation. If bulges are mostly old ([Peletier et al. 1999](#); [MacArthur et al. 2009](#))³⁵ and the more recent star formation in the galaxies has occurred in their discs, then the galaxy optical colours used thus far in this work could lead us astray. Therefore, in this section, we repeat our analysis using the latest (optical-infrared colour)-dependent M_*/L ratios. The outcome is that our main conclusion stands, reflective of the small variation in the value of M_*/L at $3.6 \mu\text{m}$.

A1 An (optical-NIR colour)-dependent Υ_*

The baseline model in [Schombert et al. \(2019, their Table 2\)](#) is such that

$$\begin{aligned} \log(M_*/L_{\text{obs},3.6}) &= 0.933(m_{V,\text{Vega}} - m_{3.6,\text{Vega}})^2 \\ &- 4.932(m_{V,\text{Vega}} - m_{3.6,\text{Vega}}) + 6.123, \end{aligned}$$

valid for $2.3 \lesssim (m_{V,\text{Vega}} - m_{3.6,\text{Vega}}) \lesssim 3.1$. This equation is based on the [Kroupa \(2001\)](#) IMF, referred to as the pseudo-Kroupa IMF by [Bernardi et al. \(2010\)](#). To adjust to the [Kroupa \(2002\)](#) IMF, one needs to subtract 0.1 dex. To use the above equation, both the V -band and the $3.6 \mu\text{m}$ magnitudes need to be calibrated on the Vega magnitude system. Given that our Spitzer $3.6 \mu\text{m}$ magnitudes are calibrated on the AB system, and the RC3 V -band data are on the Vega system, we follow [Willmer \(2018\)](#)³⁶ and use

$$m_{\text{Vega}} = m_{\text{AB}} - 2.76 \text{ mag}$$

³⁵ Old ages for (the stellar component of) bulges does not necessitate that they formed at high- z ; they could be recently built bulges made out of old stars from the progenitor galaxies in a ‘dry merger’ event, i.e., a gas-poor galaxy collision.

³⁶ <http://mips.as.arizona.edu/~cnaw/sun.html>

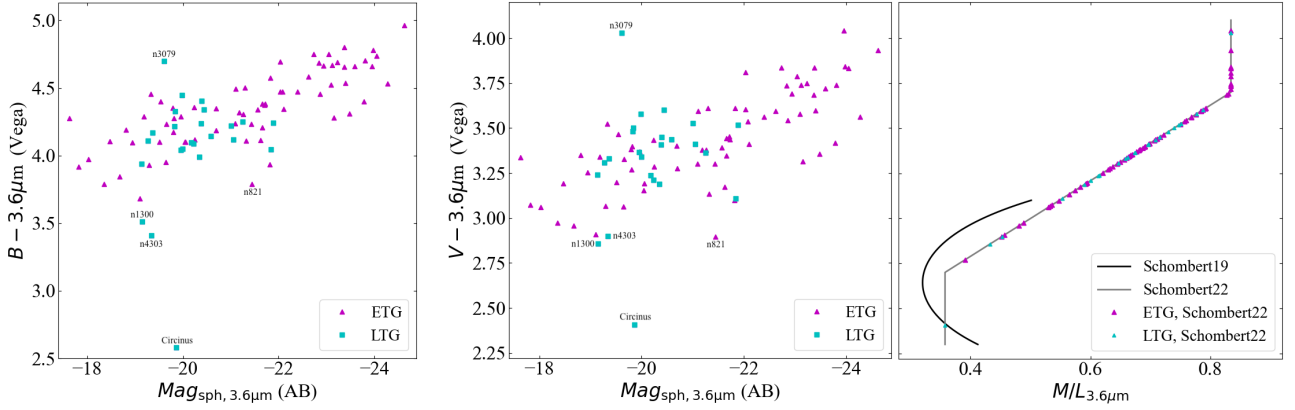


Figure A1. Left-hand and middle panel: similar to the left-hand panel of Figure 1, but showing the $m_B - m_{3.6}$ and $m_V - m_{3.6}$ (Vega) galaxy colour versus the spheroid absolute magnitude (AB). We used $m_{\text{Vega}} = m_{\text{AB}} - 2.76$ mag at $3.6 \mu\text{m}$ for the conversion. Right-hand panel: stellar mass-to-light ratios at $3.6 \mu\text{m}$ from the baseline model in Schombert et al. (2019, their Table 2) is shown by the black curve (Eq. A1) and the new prescription from Schombert et al. (2022) is shown by the grey line with triangles (Eq. A2). Both models use the $m_V - m_{3.6}$ colour and have been converted here to a Kroupa (2002) IMF. Note: The ETG with the bluest $V-[3.6]$ colour is NGC 404; it is not seen in the middle panel due to the zoomed in view.

at $3.6 \mu\text{m}$ to modify the equation such that it can use $3.6 \mu\text{m}$ (AB) and V (Vega) magnitudes. We also subtract 0.1 dex to bring it in line with the Kroupa (2002) IMF. Doing so, we have that

$$\begin{aligned} \log(M_*/L_{\text{obs},3.6}) &= 0.933(m_{V,\text{Vega}} - m_{3.6,\text{AB}} + 2.76)^2 - \\ &4.932(m_{V,\text{Vega}} - m_{3.6,\text{AB}} + 2.76) + 6.023 \end{aligned} \quad (\text{A1})$$

This relation has recently been further developed in Schombert et al. (2022), providing separate expressions for bulge and disc colours (which we do not have) and for galaxy colours which extend to redder colours than those applicable in Equation A1. We approximate the Bulge+Disc galaxy model from Schombert et al. (2022, see their Figure 3) — which is based on the Kroupa (2001) IMF — by the equations

$$\begin{aligned} M_*/L_{\text{obs},3.6} &= 0.45, \text{ for } (m_{V,\text{Vega}} - m_{3.6,\text{Vega}}) < 2.7, \\ &= 0.45 + 0.6(m_{V,\text{Vega}} - m_{3.6,\text{Vega}} - 2.7), \\ &\quad \text{for } 2.7 < (m_{V,\text{Vega}} - m_{3.6,\text{Vega}}) < 3.7, \\ &= 1.05, \text{ for } (m_{V,\text{Vega}} - m_{3.6,\text{Vega}}) > 3.7. \end{aligned}$$

Switching to the Kroupa (2002) IMF, by multiplying by $10^{-0.1} \approx 0.794$, and switching to the AB magnitude system for the $3.6 \mu\text{m}$ magnitudes, we have that

$$\begin{aligned} M_*/L_{\text{obs},3.6} &= 0.36, \text{ for } (m_{V,\text{Vega}} - m_{3.6,\text{AB}}) < -0.06, \\ &= 0.39 + 0.48(m_{V,\text{Vega}} - m_{3.6,\text{AB}}), \\ &\quad \text{for } -0.06 < (m_{V,\text{Vega}} - m_{3.6,\text{AB}}) < 0.94, \\ &= 0.83, \text{ for } (m_{V,\text{Vega}} - m_{3.6,\text{AB}}) > 0.94. \end{aligned} \quad (\text{A2})$$

We assign a 15 percent uncertainty to these, reflecting the 0.05 dex uncertainty in $\log M_*$ noted by Schombert et al. (2022) and allowing for a reasonable error in the assigned colour. This relation (Equation A2), along with Equation A1, is shown in the right-hand panel of Figure A1. One can see that they are similar over their colour range of applicability.

Comparing Figure A1 with Figure 1, it is apparent that there are some differences. For instances, while the ETGs typically have red colours and $0.6 \lesssim M_*/L_{3.6} \lesssim 0.9$ in Figure 1, they follow a colour-magnitude relation in Figure A1 and have $0.6 \lesssim M_*/L_{3.6} \lesssim 0.9$. The LTGs in Figure A1 appear to define a blue cloud, with $0.4 \lesssim M_*/L_{3.6} \lesssim 0.7$, while their cloud-like distribution appears

consistent with the ETG colour-magnitude relation in Figure A1, where they have $0.45 \lesssim M_*/L_{3.6} \lesssim 0.75$.

A few of our galaxies can also be seen to stand out in the colour-magnitude diagram shown in the left-hand and middle panels of Figure A1. The ETG with the faintest spheroid magnitude is NGC 2787, remodelled in Graham & Sahu (2022). Circinus was already discussed in Section 2.1. The Seyfert galaxy NGC 3079 is a particularly dusty and rather edge-on (80°) spiral galaxy. It is notable for having blown a rather large bubble (Cecil et al. 2001) from its central region, somewhat akin to the Fermi Bubble in the Milky Way (Sofue & Handa 1984; Su et al. 2010). de Vaucouleurs et al. (1991) suggested a dust correction of 1.1 mag to the observed B - and V -band magnitudes of NGC 3079. The infrared glow of warm dust and the reduced optical flux may have conspired to produce this outlier with an excessively red $V-[3.6]$ colour. Had the V -band magnitude been 0.5 mag brighter, this galaxy would not stand out in Figure A1 and its mass-to-light ratio would be 10 percent smaller. It does not stand out in the $M_{\text{bh}}-M_{*,\text{sph}}$ diagram. NGC 821 also appears as something of an outlier; it is too blue by ~ 0.7 mag. This may be due to contamination from the overlapping $V \approx 9.3$ mag (Vega) star SIMBAD BD+10 293.

For eight galaxies without a reliable V -band magnitude, we used a bisector regression on the available $(V-[3.6])-\mathcal{M}_{\text{sph},3.6}$ data (Figure A1) to obtain a $V-[3.6]$ colour based on their $\mathcal{M}_{\text{sph},3.6}$ values. Specifically, we derived and used the expression $V-[3.6]$ (Vega) = $1.45 - 0.09 \mathcal{M}_{\text{sph},3.6}$ (AB). These colours are marked with brackets in Table 1.

In passing, we note that, based on the pseudo-Kroupa IMF, Schombert et al. (2022) suggest $M_*/L_{\text{obs},3.6} \approx 1$ to 1.05 for elliptical galaxies, ≈ 0.97 for red bulges, which are likely in ETGs, and ≈ 0.86 for blue bulges, likely in the later spiral galaxy types. For the Kroupa (2002) IMF, this equates to 0.79 to 0.83 (E), 0.77 (red bulges), and 0.68 (blue bulges). Such a step function differs from the continuous M_*/L ratios for the galaxy models, while qualitatively mimics the approach in Sahu et al. (2019a), which used $M_*/L_{\text{obs},3.6} = 0.6$ for ETGs and 0.453 for LTGs, based on the Chabrier (2003) IMF, or 0.53 and 0.40 for the Kroupa (2002) IMF. We are, however, keen to avoid (or only use) a prescription to convert light into mass with such a discontinuity, given that we are

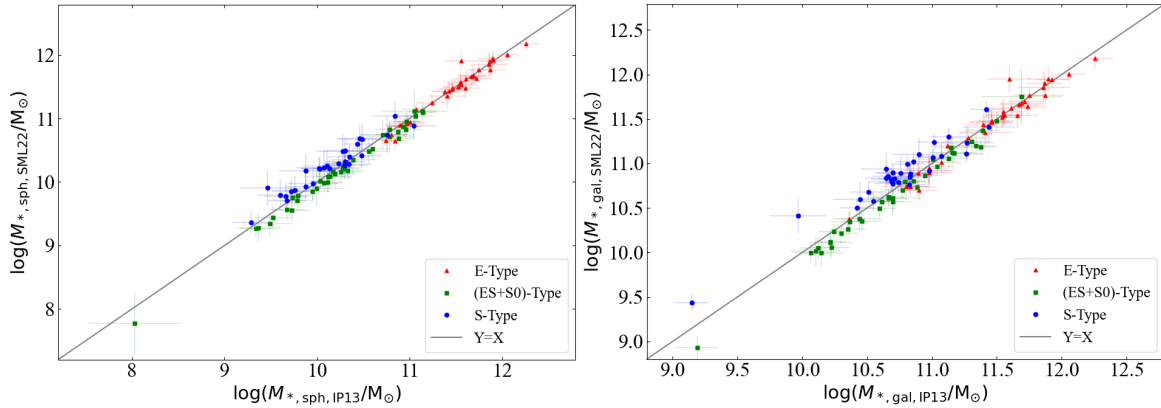


Figure A2. Comparison of the spheroid and galaxy stellar masses derived using the (optical colour)-dependent Υ_* ratios from IP13, as given by our Equation 4, and using the (optical-infrared colour)-dependent Υ_* ratios from Schombert et al. (2022), as given by our Equation A2. The differences seen here will result in different black hole scaling relations to those in the main text (Table 2).

checking for potential discontinuity or offsets in the $M_{\text{bh}}-M_{*,\text{sph}}$ diagram. We proceed using Equation A2.

Figure A2 compares the spheroid and galaxy stellar masses obtained using Equations 4 and A2. Here, one can better visualise the differences between the distribution of mass-to-light ratios seen in Figures 1 and A1. Apparently, for the full ensemble of galaxy types used in our study, the two prescriptions we have used for Υ_* — from Into & Portinari (2013) and Schombert et al. (2022) after conversion to the same IMF — yield consistent results. However, taking things to the next level by looking at dependencies on the galaxy morphology, it is also apparent that further information can be gleaned. Given the slight differences in slope and zero-point (at some mass) for each morphological type (E, ES/S0 and S), we have repeated the diagrams and analysis previously based on Equation 4.

A2 Results

It is apparent from Figure A3 that, qualitatively, the large offset between the ES/S0 and E galaxies in the $M_{\text{bh}}-M_{*,\text{sph}}$ diagram remains. That is, this is a robust result. The steeper $M_{\text{bh}}-M_{*,\text{sph}}$ relation for the bulges of spiral galaxies is in agreement with that observed when using $M_*/L_{\text{obs}} = 0.453$ for every spiral galaxy with *Spitzer* data (Davis et al. 2019). This may seem counterintuitive until it is remembered that this recent study included additional non-*Spitzer* data, plus we have updated some of the photometric decompositions. The results suggest that the evolution of bulges in relatively gas-poor versus gas-rich discs may proceed along different paths, converging at high bulge masses (Figure A3, middle panel). Perhaps stellar feedback has limited the black hole accretion in the spiral galaxies, explaining their lower $M_{\text{bh}}/M_{*,\text{sph}}$ ratios than in many similarly-massed ES/S0 galaxy bulges. Alternatively, perhaps the black holes in the spiral galaxies are yet to grow up by exhausting their fuel supply and largely drying out, as has occurred in many of the ES/S0 galaxies.

Using Equation A2, the $M_{\text{bh}}-M_{*,\text{gal}}$ relations have also been re-derived for the E, ES/S0, and S galaxies (Figure A5), as has the associated $(M_{\text{bh}}/M_{*,\text{gal}})-M_{*,\text{gal}}$ diagram (Figure A6). Table A1 provides the mass scaling relations based on Equation A2. Of note is the ~ 0.3 dex, nearly 2σ , change to the intercept of the $M_{\text{bh}}-M_{*,\text{gal}}$ relation for the spiral galaxies. This translates to predictions for black hole masses in spiral galaxies that are a factor of ~ 2 different to what one obtains when using the scaling relations in the main

text. This highlights the need to pay attention to the ν term in these equations.

The spheroid size-mass diagram has been reproduced in Figure A7 using the stellar mass-to-light ratios obtained via Equation A2. It continues to reveal an apparent continuity between bulges and elliptical galaxies that supports the merger-built evolutionary process (shown in Figures A4 and A6) for explaining the demographics of massive ETGs in the $M_{\text{bh}}-M_{*,\text{sph}}$ diagram.

Building on Figure 9, Figure A8 shows additional pathways for the bulges of spiral galaxies. While we have introduced colour-dependent M_*/L ratios and provided a previously absent interpretation for the $M_{\text{bh}}-M_{*,\text{sph}}$ and $M_{\text{bh}}-M_{*,\text{gal}}$ diagrams, we identify areas where further improvement can be pursued. This includes the derivation of bulge, rather than galaxy, colours. These may come from the decomposition of optical images or sampling regions of the bulge largely unaffected by dust (e.g., Balcells & Peletier 1994). Furthermore, with integral field units (IFUs), one can pursue star formation histories and rates, extinction, metallicity and ages (e.g., García-Benito et al. 2019, and references therein) on a spaxel-by-spaxel basis. Of course, some kind of bulge/disc separation will still be desirable for many spaxels, just as it is when dealing with a global galaxy colour. Nonetheless, these measurements should enable refined stellar M_*/L ratios for the bulges, which will help to better establish the LTG bulge sequence in the $M_{\text{bh}}-M_{*,\text{sph}}$ diagram. Understanding the potential offset between the bulges of LTGs and the bulges of ETGs offers the promise of yet further insight into the intriguing lives of galaxies and their black holes. Colour and metallicity gradients (e.g., Spolaor et al. 2009) may also offer clues to how some systems formed, whether through wet or dry mergers or relics from an early-Universe. Here, we have implicitly focussed on dry mergers in which the bulk of the orbital angular momentum (both in the progenitors and between them) cancels and an E galaxy is generated. We will explore merger-built systems that have retained substantial angular momentum in Graham & Sahu (2022).

A3 Some notes on little ν

Here, we discuss the mass-to-light conversion term, ν , introduced in Davis et al. (2019), and further developed in Sahu et al. (2019a), to account for switches between various prescriptions of Υ_* (e.g., Bell et al. 2003; Zibetti et al. 2009; Taylor et al. 2011; Into & Porti-

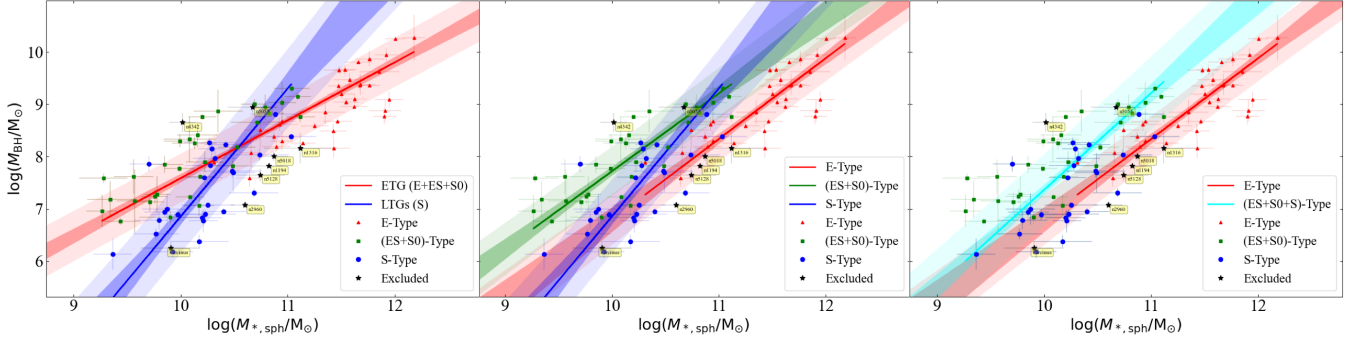


Figure A3. Similar to Figure 2 but using Equation A2 to derive the spheroid stellar masses. This yields black hole scaling relations with similar relative offsets to those seen in Sahu et al. (2019a), which used $M_*/L_{s,3.6} = 0.6$ for all, after applying a 25 percent reduction to the LTGs' luminosity $L_{obs,3.6}$ due to dust glow in the LTGs (Querejeta et al. 2015). Here, the middle panel appears to be the optimal separation of morphological types. The bulges of spiral galaxies and lenticular galaxies appear to converge at high masses.

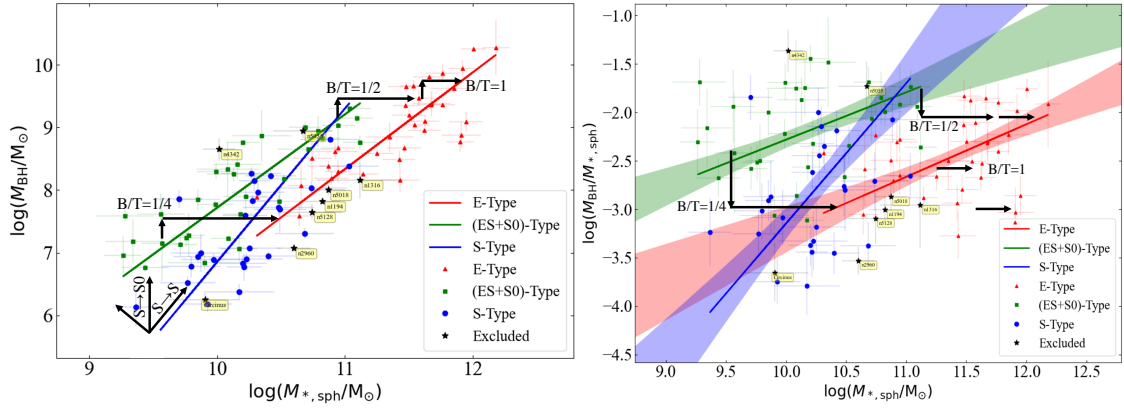


Figure A4. Left-hand panel: Similar to the right-hand panel of Figure 8 but using Equation A2 to derive the spheroid stellar masses and with the shading removed. Right-hand panel: Similar to Figure 3 but using Equation A2. The lines have been propagated from the middle panel of Figure A3. For a given spheroid mass, the average $M_{bh}/M_{*,sph}$ ratio depends on the galaxy's morphological type and thus formation history.

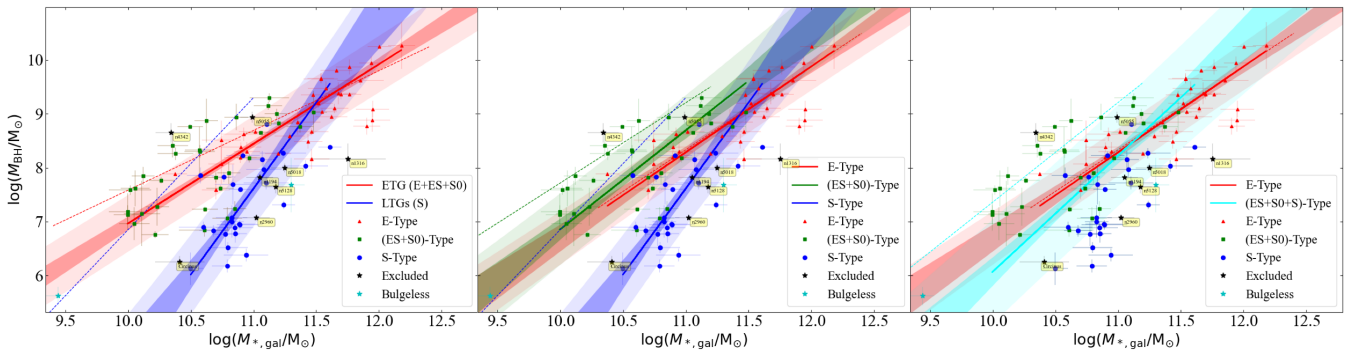


Figure A5. Similar to Figure 5, but using Equation A2. The solid lines show the galaxy relations while the dashed lines show the associated spheroid relations from Figure A3.

nari 2013; Roediger & Courteau 2015; Schombert et al. 2022).³⁷

³⁷ The lower-case upsilon symbol was introduced to facilitate changes to the mass-to-light ratio, Υ_* , in a similar manner to how h can enact changes to the adopted Hubble-Lemaître constant H_0 .

Such conversions are necessary if one uses any $M_{bh}-M_{*,sph}$ and/or $M_{bh}-M_{*,gal}$ scaling relations when an alternative Υ_* prescription to that used to establish these relations is used to obtain the stellar mass of the target for which one wishes to predict the black hole mass. While this should sound obvious, it can be problematic in practice and Sahu et al. (2022b) show how failing to do so can

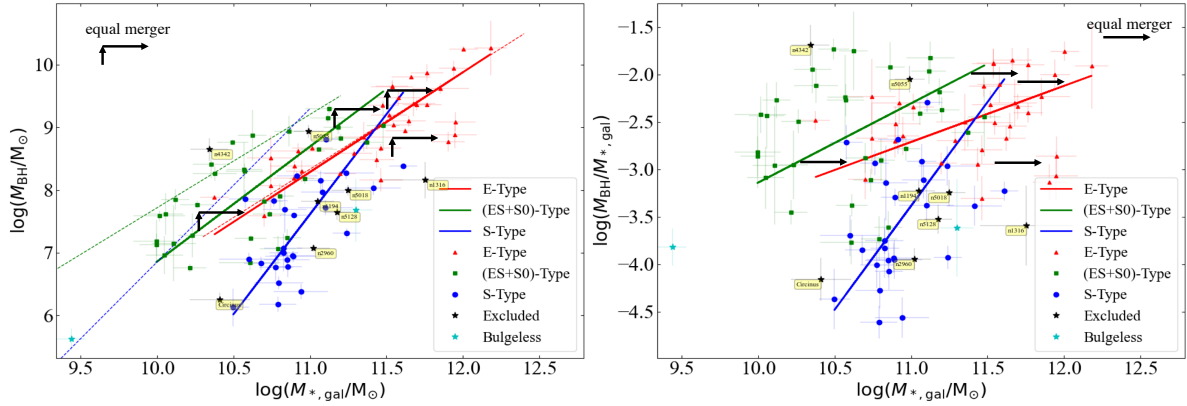


Figure A6. Left-hand panel: Similar to the middle panel of Figure A5 but without the shading. Right-hand panel: Similar to Figure 6, but using Equation A2. The lines have been propagated from the middle panel of Figure A5. The arrows show the movement due to a dry equal-mass merger.

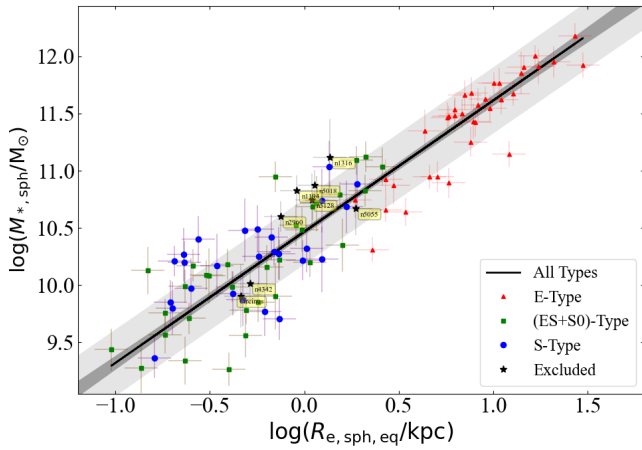


Figure A7. $R_{e,sph,eq}$ versus $M_{*,sph}$. Similar to Figure 7 but using Equation A2 for the spheroid masses.

Table A1. Black hole mass scaling relations

Galaxy type	Slope (A)	Intercept (B)	Δ_{rms}
$\log(M_{bh}/M_{\odot}) = A \log[M_{*,sph}/\nu(5 \times 10^{10} M_{\odot})] + B$			
E (35)	1.54 ± 0.16	7.87 ± 0.17	0.41
ES/S0 (32)	1.49 ± 0.16	8.76 ± 0.17	0.45
S (26)	2.45 ± 0.49	8.56 ± 0.29	0.67
ES/S0 & S (58)	1.85 ± 0.18	8.66 ± 0.15	0.67
E & ES/S0 (67)	1.11 ± 0.07	8.36 ± 0.11	0.45
$\log(M_{bh}/M_{\odot}) = A \log[M_{*,gal}/\nu 10^{11} M_{\odot}] + B$			
E (35)	1.59 ± 0.17	8.29 ± 0.14	0.42
ES/S0 (32)	1.83 ± 0.26	8.70 ± 0.19	0.62
S (26)	3.19 ± 0.55	7.62 ± 0.16	0.67
ES/S0 & S (58)	2.15 ± 0.27	8.23 ± 0.13	0.92
E & ES/S0 (67)	1.48 ± 0.10	8.45 ± 0.11	0.51
$\log(M_{sph}/\nu M_{\odot}) = A \log[R_{e,sph,eq}/kpc] + B$			
All (93)	1.15 ± 0.05	10.47 ± 0.08	0.28

Similar to Table 2 but the stellar masses used to derive the relations shown here came from Equation A2. As such, when using these equations, $\nu = 1$ if one uses stellar masses consistent with those obtained via Equation A2.

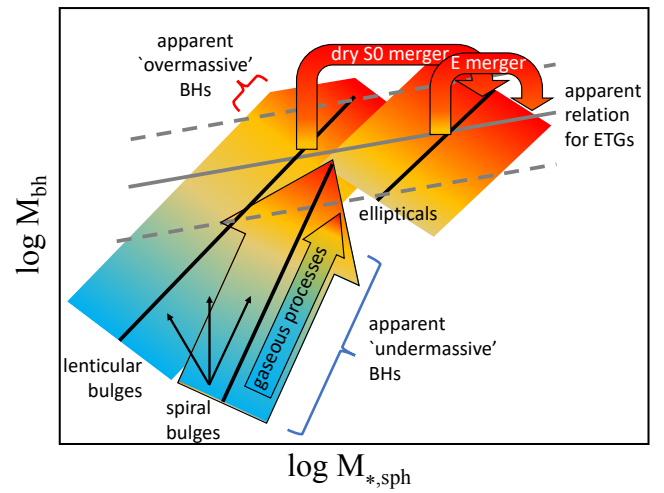


Figure A8. Modification of Figure 9. The band on the left shows the relation for bulges in lenticular galaxies while the steeper band in the middle is for the bulges of spiral galaxies, and the band on the right shows the relation for elliptical galaxies. The shallower relation, shown in grey, tracks an apparent ‘red sequence’, or equally ‘red herring’. Regarding the three thin arrows in the lower part of the diagram: if the gaseous evolution of spiral galaxies predominantly grows the disc and AGN but not the bulge, then it will evolve upwards in this diagram rather than along the spiral galaxy sequence. Alternatively, mass loss from stellar winds may fuel the AGN and decrease the spheroid stellar mass.

result in a bias, explaining the offset presented in Shankar et al. (2016) and the incorrect conclusion that galaxies with directly observed black hole masses are offset from the SDSS population of ETGs in the $M_{bh}-\sigma$ diagram.

We raised awareness of this general issue in Davis et al. (2019, their Eq. 10), through the introduction of the ν term in the relation $\log(M_{bh}) = A \log(M_*/\nu) + B$. Davis et al. (2019) used $M_*/L_{obs,3.6} = 0.453$ for a sample of spiral galaxies imaged with the Spitzer Space Telescope’s Infrared Array Camera - channel 1 (IRAC-1: Fazio et al. 2004), which operated at a central wavelength of $3.6 \mu m$. As such, ν was initially introduced as $\nu_{IRAC1,0.453} = Y_{IRAC1}/0.453$, with Y_{IRAC1} a (potentially) different stellar mass-to-light ratio used by someone else to obtain the stellar masses of their spheroid and/or

galaxy sample. Sahu et al. (2019a, their Figure 4 and their Equations 6–8 for ν) developed this further by providing a limited set of conversions for when the user of the scaling relation has obtained their stellar mass in a non-IRAC1 band and thus does not simply have an alternate Υ_{IRAC1} value.

There are multiple approaches to deriving ν , and we present two of them here, using the Υ_* prescriptions given in this paper as an example.

From its definition, we have that

$$\nu \equiv \Upsilon_2 / \Upsilon_1, \quad (\text{A3})$$

for use in an expression like

$$\log(M_{\text{bh}}/M_{\odot}) = A_1 \log[M_{*,\text{sph},1}/\nu(5 \times 10^{10} M_{\odot})] + B_1 \quad (\text{A4})$$

in which Υ_1 was used to define $M_{*,\text{sph},1}$. Now, if, for example, one uses Equation A2 to derive the stellar mass of a spheroid, but wishes to use the equations from Table 2, then one can calculate the required ν term by dividing the Υ_2 ratio from Equation A2 by that given in Equation 4, to give

$$\nu = \frac{0.39 + 0.48(m_{V,\text{Vega}} - m_{3.6,\text{AB}})}{10^{1.034(m_{B,\text{Vega}} - m_{V,\text{Vega}}) - 1.067}}, \quad (\text{A5})$$

for $-0.06 < (m_{V,\text{Vega}} - m_{3.6,\text{AB}}) < 0.94$ and $m_{B,\text{Vega}} - m_{V,\text{Vega}} > 0.5$. This is fine if one has both of these colour terms, with the two magnitudes required for each colour being measured consistently, for example, within the same aperture. However, this information may not be available, in which case an alternative method is required.

A second approach uses the scaling relation obtained by comparing the masses, M_1 and M_2 , of other spheroids obtained using each of the M_*/L ratios. An example of this is seen in Figure A2. For the relation

$$\log[M_2/(5 \times 10^{10} M_{\odot})] = a \log[M_1/(5 \times 10^{10} M_{\odot})] + b, \quad (\text{A6})$$

it can be shown that

$$\log \nu = \left(\frac{a-1}{a} \right) \log[M_2/(5 \times 10^{10} M_{\odot})] + b/a. \quad (\text{A7})$$

Thus, knowing a and b provides an alternative means to calculate the value of ν for your value of M_2 obtained using Υ_2 .

The slightly different trends in Figure A2 resulted in the somewhat different black hole scaling relations between Table 2 and Table A1. With a little algebra, it can also be shown that

$$a = \frac{2A_1}{A_1 + A_2} \text{ and } b = \frac{B_1 - B_2}{A_1 + A_2}, \quad (\text{A8})$$

where A_1 and B_1 are the slope and intercept from the black hole scaling relation (Table 2) derived using the Υ_1 ratios (Equation 4) and A_2 and B_2 are the slope and intercept from the black hole scaling relation (Table A1) derived using the Υ_2 ratios (Equation A2). For our spiral galaxies, for example, we have from Equation A8 that $a = 0.96$ and $b = 0.02$, while for our ES/S0 galaxies, we have $a = 1.01$ and $b = -0.03$. Such morphology-specific terms for the ν equation (Equation A7) provide an additional level of sophistication to that presented in Sahu et al. (2019a).

This paper has been typeset from a \LaTeX file prepared by the author.